The thermal equation of state of xenon: Implications for noble gas incorporation in serpentine minerals and their transport to depth

Angelika D Rosa, F Zecchi, Pierre Condamine, Mohamed Ali Bouhifd, Joao Elias Figueiredo Soares Rodrigues, E Mijit, Tetsuo Irifune, O Mathon, G Garbarino, Mohamed Mezouar, et al.

Geochimica et Cosmochimica Acta 378 (2024) 99–113

Contents lists available at ScienceDirect

Geochimica et Cosmochimica Acta

journal homepage: www.elsevier.com/locate/gca

The thermal equation of state of xenon: Implications for noble gas incorporation in serpentine minerals and their transport to depth

A.D. Rosa [a,*], F. Zecchi [a], P. Condamine [b], M.A. Bouhifd [b], J.E.F.S. Rodrigues [a], E. Mijit [a], T. Irifune [c], O. Mathon [a], G. Garbarino [a], M. Mezouar [a], A. Dewaele [d,f], N. Ishimatsu [c,e]

[a] European Synchrotron Radiation Facility, ESRF, Grenoble, France
[b] Laboratoire Magmas et Volcans, Université Clermont Auvergne, CNRS, IRD, OPGC, F-63000 Clermont-Ferrand, France
[c] Geodynamics Research Centre, Ehime University, 2-5 Bunkyo-cho, Matsuyama 790-8577, Japan
[d] CEA, DAM, DIF, 91297 Arpajon Cedex, France
[e] Graduate School of Advanced Science and Engineering, Hiroshima University, Higashihiroshima, Hiroshima 739-8526, Japan
[f] Université Paris-Saclay, CEA, Laboratoire Matière en Conditions Extrêmes, 91680 Bruyères-le-Châtel, France

ARTICLE INFO

Associate editor: Manuel Moreira

Keywords:
Noble gases
Subduction
Serpentine minerals
High pressure experiments
Crystal chemical modelling

ABSTRACT

Isotopic signatures of heavy noble gases in the Earth's mantle contain a major component recycled by subduction. The experimental and field studies reported in the literature show increasing evidence that serpentine minerals can hold large quantities of noble gases, potentially serving as their primary vectors to depth. However, at present, their retention mechanism in these minerals is not fully understood. Additionally, noble gas solubilities from field and experimental studies show large differences in terms of elemental concentrations. Here, we performed crystal chemical modeling to evaluate the incorporation mechanism of noble gases and their solubilities in serpentine minerals along subduction zone geotherms. To this end, we determined the thermal equation of state of xenon using *in situ* X-ray diffraction and absorption up to 60 GPa and 728 K. In this range, the xenon equation of state is well-adjusted using the Mie-Grüneisen-Debye formalism with relevant fitting parameters. We show that the experimentally observed solubility trend, which follows the order Ne < He < Ar < Kr < Xe, can be explained by the incorporation of noble gases at two distinct crystallographic sites. The light noble gases He and Ne are most likely retained at the van der Waals hydrogen-oxygen bond position between the layers, while the heavy and larger noble gases enter the voids between the six-membered SiO_4 rings. It should be noted that octahedral sites can potentially host xenon, but cannot accommodate argon and krypton. Indeed, this would require unrealistic flexibility of the crystal lattice. Our models extended to mantle wedge conditions predict decreasing solubilities, particularly for light noble gases, in agreement with observations from natural samples. Compared to the noble gas concentrations determined experimentally in serpentine, natural concentrations are much higher and very variable. Our solubility model confirms that equilibrium processes cannot explain these observations. We therefore suggest that the high and variable noble gas concentrations found in natural samples must be due to hybrid hydration processes in ultramafic rocks that involve different degrees of water activities.

1. Introduction

Noble gases are powerful trace elements for reconstructing the chemical evolution of the mantle over geological time. Their mantle concentration depends on the mass balance between degassed noble gases (mainly by volcanism) and ingassed fluxes (*via* subduction of hydrothermally altered oceanic lithosphere). A growing number of studies support the scenario of a replenishment of mostly Ar, Kr and Xe in the mantle by the recycling of surface noble gases, i.e., their entrainment and retention in the mantle *via* subduction, while regassing of He and Ne in the mantle via subduction is considered negligible (Moreira, 2013; Mukhopadhyay and Parai, 2019). However, the mechanisms of heavy noble gas entrainment and retention in slabs remain debated (Sarda, 2004; Holland and Ballentine, 2006; Kendrick et al., 2011; Péron and Moreira, 2018; Krantz et al., 2019). Here, the central open questions are: 1) what is the mechanism of noble gas incorporation into hydrous

* Corresponding author.
E-mail address: angelika.rosa@esrf.fr (A.D. Rosa).

https://doi.org/10.1016/j.gca.2024.06.001
Received 12 December 2023; Accepted 1 June 2024
Available online 15 June 2024

subduction zone minerals and 2) what is the origin of the differences observed between the concentrations of noble gas determined experimentally and those found in natural samples? The present work aims at deepening our knowledge on the subduction recycling mechanism of noble gases *via* altered peridotitic lithologies with a particular emphasis on the main hydrous phases they contain, *i.e.* lizardite (Lz) and antigorite (Atg).

These minerals, also referred to as serpentine polymorphs, can contain up to 13 wt% of water (ideal formula $Mg_3Si_2O_5(OH)_4$) and are composed of alternating sheets of edge-sharing MgO_6 octahedra and corner-shared SiO_4 tetrahedra forming six membered rings. These structures exhibit a high flexibility and contain open voids that are ideal for the incorporation of trace elements (Deschamps et al., 2013; Lafay et al., 2013; Jackson et al., 2015). Due to their high chemical stability over an extended *P/T* domain, they can carry crystalline bound water and potentially other trace elements beyond the depth of arc magmas (Poli and Schmidt, 2002; Scambelluri et al., 2019; Ohtani, 2020). Lz is the low-pressure polymorph that forms during the reaction between water, olivine and enstatite at hydrothermal or abyssal conditions below 573 K and 0.12 GPa in seafloor peridotites, deep thrust faults, or accretionary wedge from slab derived fluids. Atg is the high-pressure polymorph forming at greater depth in subduction zones from Lz through dissolution and recrystallization ($T > 573$ K, $P > 0.08$ GPa) (Auzende et al., 2006).

Major evidence for the replenishment of noble gases into the mantle via subduction come from field studies. Notably, the isotopic noble gas compositions of krypton (Kr) and xenon (Xe) in the source of MORBs (mid ocean ridge basalts) and mantle-derived CO_2-wells contain a dominant atmospheric-like component, which can reach up to 92 % for ^{130}Xe in MORBs (Staudacher and Allègre, 1988; Holland and Ballentine, 2006; Ballentine and Holland, 2008; Parai and Mukhopadhyay, 2015). Regassing of heavy noble gases into the mantle has also been evidenced for the OIB mantle sources (Peto et al., 2013; Parai and Mukhopadhyay, 2015; Péron and Mukhopadhyay, 2022), and, more specifically, the proportion of recycled atmospheric Kr has been refined by Péron and Mukhopadhyay (2022). These observations and the strong correlation of the noble gas isotopic signatures of MORBs with isotopic signatures of halogens and fluid mobile elements suggest that recycled materials have been integrated into the MORB source (Chauvel et al., 1992; Moreira et al., 1998; Sarda et al., 1999; Holland and Ballentine, 2006; Rapp et al., 2008; Parai and Mukhopadhyay, 2015). Similar conclusions can be drawn from the elemental noble gases abundance ratios (Kr/Ar and Xe/Ar) of the MORB and OIB sources that are greater than those of the atmosphere and, quite similar to those of seawater (Hanyu et al., 1999; Trieloff et al., 2000; Ballentine and Holland, 2008; Kendrick et al., 2011). The enrichment of the MORB source in heavy noble gases cannot therefore be explained by the simple mixing between atmosphere and seawater (Moreira et al., 1998; Holland and Ballentine, 2006). Interestingly, oceanic plate lithologies including sediments, altered oceanic crust (AOC) and serpentinized peridotite of the lithospheric mantle exhibit similar or even higher Xe/Ar and Kr/Ar ratios than the MORB source (Matsuda and Nagao, 1986; Staudacher and Allègre, 1988; Kendrick et al., 2011, 2013; Chavrit et al., 2016; Kendrick et al., 2017, 2018). In addition, altered oceanic plate lithologies are enriched in noble gases relatively to the mantle (reaching up to three orders of magnitude greater enrichment, except for helium) (Kendrick et al., 2011; Chavrit et al., 2016). Based on the observations listed above and the fact that the heavy noble gas (Kr, Xe) isotopic composition of the MORB and OIB mantle sources are distinct from seawater/air (Holland et al., 2009; Péron and Moreira, 2018; Péron and Mukhopadhyay, 2022), their recycling into the mantle could explain the observed noble gas isotopic and elemental ratios of MORBs on OIBs. The reported isotopic composition of $^{38}Ar/^{36}Ar$ in the MORB and OIB mantle sources are nearly indistinguishable from air (Raquin and Moreira, 2009) and, therefore, the use of the isotopic signature of Ar is less relevant with regard to subduction processes. Several studies recently reported direct evidence for noble gas subduction through serpentinized peridotite (Sumino et al., 2010; Kendrick et al., 2011; Kendrick et al., 2013; Kobayashi et al., 2017; Kendrick et al., 2018). These works showed a progressive reduction of noble gas concentrations with increasing subduction metamorphism indicating that most of noble gases (~80 %) are lost from the slab, while a small fraction of noble gases (~20 %) can be captured in the breakdown residue of serpentine minerals.

Few experimental studies confirmed the high solubilities of noble gases in hydrous or anhydrous minerals contained in subducting slab lithologies, including amphiboles, antigorite and magnetite (Lancet and Anders, 1973; Zaikowski and Schaeffer, 1979; Jackson et al., 2013; Jackson et al., 2015; Krantz et al., 2019). However, the noble gas concentrations predicted from the experimental solubility data are far lower than those observed in natural rocks. For example, Zaikowski and Schaeffer (1979); (Krantz et al., 2019) reported partitioning coefficients K_i that range between 0.0006 and 0.01 with K_i = [*mol/g* serpentine]/[*mol/g* water]. This would imply concentrations of 9–0.5 * 10^{-17} mol/g for ^{130}Xe dissolved at equilibrium in antigorite at 0.1 GPa by seawater serpentinization (Krantz et al., 2019). In contrast, studies on seafloor serpentines and deeply subducted antigorites reported much higher concentrations, i.e. 1.4–1.1 * 10^{-15} mol/g of ^{130}Xe (Kendrick et al., 2011; Kendrick et al., 2013).

While the elemental fractionation pattern observed in natural samples could be reproduced experimentally, showing higher solubilities of heavy noble gases compared to light NGs, the incorporation mechanism of noble gases in the crystal structure remains controversial. Indeed, several scenarios have been proposed including their favoured absorption in crystal structures, their lower diffusivities in seawater and crystals, or the observed higher solubilities of Kr and Xe relatively to helium (He), neon (Ne) and argon (Ar) in serpentinite minerals (Lancet and Anders, 1973; Zaikowski and Schaeffer, 1979; Krantz et al., 2019; Wang et al., 2020).

Here, we used a crystal-chemical approach to model the incorporation and solubility variations of noble gases in lizardite and antigorite. This approach relies on the well-established empirical relation between the solubility behaviour of an element in a crystalline phase and its atomic radii and valence (Blundy and Wood, 2003). Since noble gases are charge neutral, their compatibility in vacancy sites of the host phase is mainly controlled by their atomic radii (Brooker et al., 2003; Heber et al., 2007b; Shcheka and Keppler, 2012; Rosa et al., 2020) and incorporation energies (Thompson and Wolverton, 2011). The precise knowledge of the thermo-elastic parameters of noble gases and host phases is a prerequisite for these models. However, those data are scarce for the heavy noble gases and, more particularly for Xe due its very low thermal expansion. For Ar, Kr and Xe only two experimental studies have been carried-out to collect volumetric data at high pressure and high or low temperature (Anderson and Swenson, 1975; Jephcoat, 1998). However, the thermo-elastic parameters resulting from these works differ greatly. Indeed, for Ar, Kr and Xe, the reported bulk moduli (K_0), their first derivatives (K'_0), the Debye temperatures (Θ_D) and, Grüneisen parameters (γ_0) differs by up to 15 %, 40 %, 9.6 %, and 19 %, respectively. These discrepancies are much larger than the experimental uncertainties that are typically of 1 % for K_0 and K'_0 and, 4 % for Θ_D and γ_0. They may arise from the different experimental techniques used for volume determination (*e.g.*, variation of piston position versus X-ray diffraction), or from the progressive pressure induced face centred cubic (fcc) to the hexagonal closed pack (hcp) structure phase transition in pure solid Xe, Kr and Ar that alters their compression behaviours (Rosa et al., 2018; Dewaele et al., 2021; Rosa et al., 2022). This fcc-hcp martensitic transition, is a diffusionless transformation that progresses over a large pressure interval through the formation of hcp stacking faults in the fcc phase formed by the collective shuffling of atoms in closed packed lattice planes. Similarly to the hardening effects associated to the martensitic transition in steels, the presence of stacking faults alters the mechanical properties of the fcc phase of noble gas solids (Rosa et al., 2018; Dewaele et al., 2021; Rosa et al., 2022). Based on

reported thermal equation of state (EOS) data, the calculated zero-charged Xe radii at cold subduction zone conditions would vary between 1.61 to 1.56 Å (100 km depth, 3.5 GPa, 773 K, with 10 coordinating atoms). Using lattice strain modelling (see methods section), these atomic radii differences lead to solubility differences of up to one order of magnitude for ^{130}Xe in antigorite. In order to reduce uncertainties on the thermo-elastic properties of Xe, we conducted high-precision volumetric measurements on pure xenon at simultaneous high *P/T* conditions up to 728 K and 60 GPa across the fcc to hcp martensitic transition. This allowed us to model the incorporation mechanism of Xe in lizardite and antigorite at subduction zone conditions. Based on our previously determined thermo-elastic data for Ar (Dewaele et al., 2021) and the refined EOS of Kr (Rosa et al., 2018), we applied the lattice strain model to the suite of heavy noble gases that could well-reproduce the experimentally observed solubility patterns and proposed two different incorporation sites for light and heavy noble gases in serpentine minerals. We discuss the implications of our findings regarding the entrainment of noble gases in seafloor peridotite and, through this lithology into the deep mantle.

2. Methods

2.1. High pressure and high temperature experiments

We conducted four high *P/T in situ* X-ray diffraction (XRD) and absorption spectroscopy (XAS) runs on pure xenon at the European Synchrotron Radiation Facility (ESRF) (Raimondi et al., 2023). Runs 1–3 were conducted at the high-pressure XRD beamline ID15B and devoted to the determination of the thermo-elastic properties and the progression of the fcc to hcp phase transition of solid xenon. Run 4 was performed at the XAS beamline BM23 and focused on the study of the bonding strength and vibrational properties of solid xenon at high *P/T*. As these instruments provide a high photon flux, highly focused beams and state-of-the-art detection systems, these beamlines are ideally suited for this type of studies (Mathon et al., 2015; Poręba et al., 2023). A summary of the experimental conditions is listed in Table 1. For the precise determination of the thermal EOS parameters, it was necessary to determine the lattice volume of solid xenon up to very high pressures of 60 GPa and with a large number of collected data points for each isotherm (more than 120 collected data points).

The high pressure conditions were generated using Letoullec-type (Letoullec et al., 1988) membrane diamond anvil cells (DACs) available at the ESRF sample environment unit. Single-crystal diamond anvils with culet sizes ranging from 250 to 300 μm were employed for the 3 XRD runs (run 1–3). Nano-polycrystalline diamond anvils with 600 μm were used for the XAS run (run 4) to ensure the collection of high quality glitch-free XAS data (Ishimatsu et al., 2012; Rosa et al., 2019). For all experiments, rhenium was employed as gasket material. The sample chamber consisted of a cylindrical hole drilled at the centre of the gasket indentation using a pulsed YAG laser. High-purity (99.99 %) xenon gas from the company Nippon was loaded into the sample cavity using the ESRF gas-loading system. Stable high temperatures up to 728 K were generated using a resistively heated ring placed around the DACs inside a vacuum vessel equipped with large X-ray transparent windows. A gold chip and a ruby sphere were placed in the sample chamber for pressure determination at high temperature (Anderson et al., 1989; Shen et al., 2020). For the XAS run, a powder of Sm doped strontium borate was used as pressure sensor (Figure S1) because of its high pressure and low temperature sensitivity (Romanenko et al., 2018).

Table 1
Information regarding the XRD and XAS runs conducted on pure xenon in this study.

Run	X-ray probe	Beamline	Beamsize (μm^2)	Temperature (K)	Pressure (GPa)	Data points
1	XRD	ID15b	10x10	429	0.7–18	128
2				568	2–58.2	252
3				728	2.7–53.2	184
4	XAS	BM23	3x3	393–623	0.2–5	21

2.2. X-ray diffraction measurements

Monochromatic X-ray diffraction (XRD) measurements were performed at the beamline ID15B. The incident X-ray beam energy was fixed to 30.1 keV (λ = 0.411909 Å) using a cryo-cooled silicon (1 1 1) monochromator. The intense X-ray beam was focused down to a 10x10 μm^2 spot using compounds refractive lenses made of aluminium. The 2-dimensional powder XRD images were collected using a large area image plate detector model MAR345. The sample to detector distance and detector tilt angles that served as integration parameters were accurately determined using a silicon powder standard. This standard whose lattice parameters are known with high precision, as well as the observed deviation from the circularity of the Debye-Scherrer rings were used to extract these parameters. Typical exposure times of 1–2 s were employed to collect high-quality XRD data. All XRD images were integrated into 72 azimuthal slices and analysed using Rietveld refinement as implemented in the software package MAUD (Lutterotti et al., 1997). Using this integration procedure, the pressure evolution of the structure, preferred orientations and microstructural were monitored *in situ*. An example of raw diffraction data and the corresponding refinement are shown in Figure S2. Refined sample parameters included lattice parameters, volume fractions and crystal domain sizes for both the fcc and hcp phase of xenon. The experimental results are listed in Table S1. The lattice parameters of the gold standard were extracted by Rietveld refinement of the 1-dimensional powder XRD data and used to determine the sample pressure using the thermal equation of state of gold reported by Anderson et al. (1989). The uncertainty on the pressure determination ranged between 5 and 10 % (Table S1).

The pressure gradients were characterized using the XRD patterns of the gold pressure sensor by quantifying the slight deviation of the Bragg reflections positions to the ideal ones for a cubic symmetry. This was achieved using the well-established procedure developed by Takemura & Dewaele (Takemura and Dewaele, 2008). For all high temperature runs, the non-hydrostatic stress components were lower than 0.1 GPa (Figure S3). This negligible value is well below that reported for Ar and Xe at room temperature (Dewaele et al., 2019; Dewaele et al., 2021) and comparable to that determined for He (Takemura and Dewaele, 2008), the most hydrostatic pressure medium (Klotz et al., 2009).

The evolution of the (1 1 1) and (2 0 0) fcc Bragg reflections of xenon across the pressure- and temperature- induced fcc-hcp martensitic transition for runs 2 and 3 at 568 K and 728 K, respectively, is shown in Fig. 1. At low pressure, both reflections have a well-defined circular shape and, their intensity maxima are spatially localized. This observation is indicative of a high-degree of crystalline order and the absence of defects, attesting that at these pressure and temperature conditions fcc xenon forms a high-quality single-crystal. Upon increasing pressure, a pronounced X-ray diffuse scattering signal appears in the vicinity of the (1 1 1) Bragg reflection and, between the (1 1 1) and (2 0 0) reflections. This has been reported previously (Cynn et al., 2001; Errandonea et al., 2002) and interpreted as a signature of the formation of hcp stacking faults in single-crystalline fcc xenon. With increasing pressure (e.g., at 10.2 GPa in run 2 and 8.4 GPa in run 3), the intensity of the X-ray diffuse scattering signal increases at diffraction angles corresponding to the hcp phase. This confirms the progressive nature of the fcc-hcp phase transformation and, the formation of a powder-like hcp phase.

2.3. X-ray absorption spectroscopy measurements

Xenon K-edge X-ray absorption spectroscopy (XAS) data were acquired at the beamline BM23 up to a *k*-range of 12 Å^{-1}. More details regarding the optical configuration of the BM23 can be found in Mathon

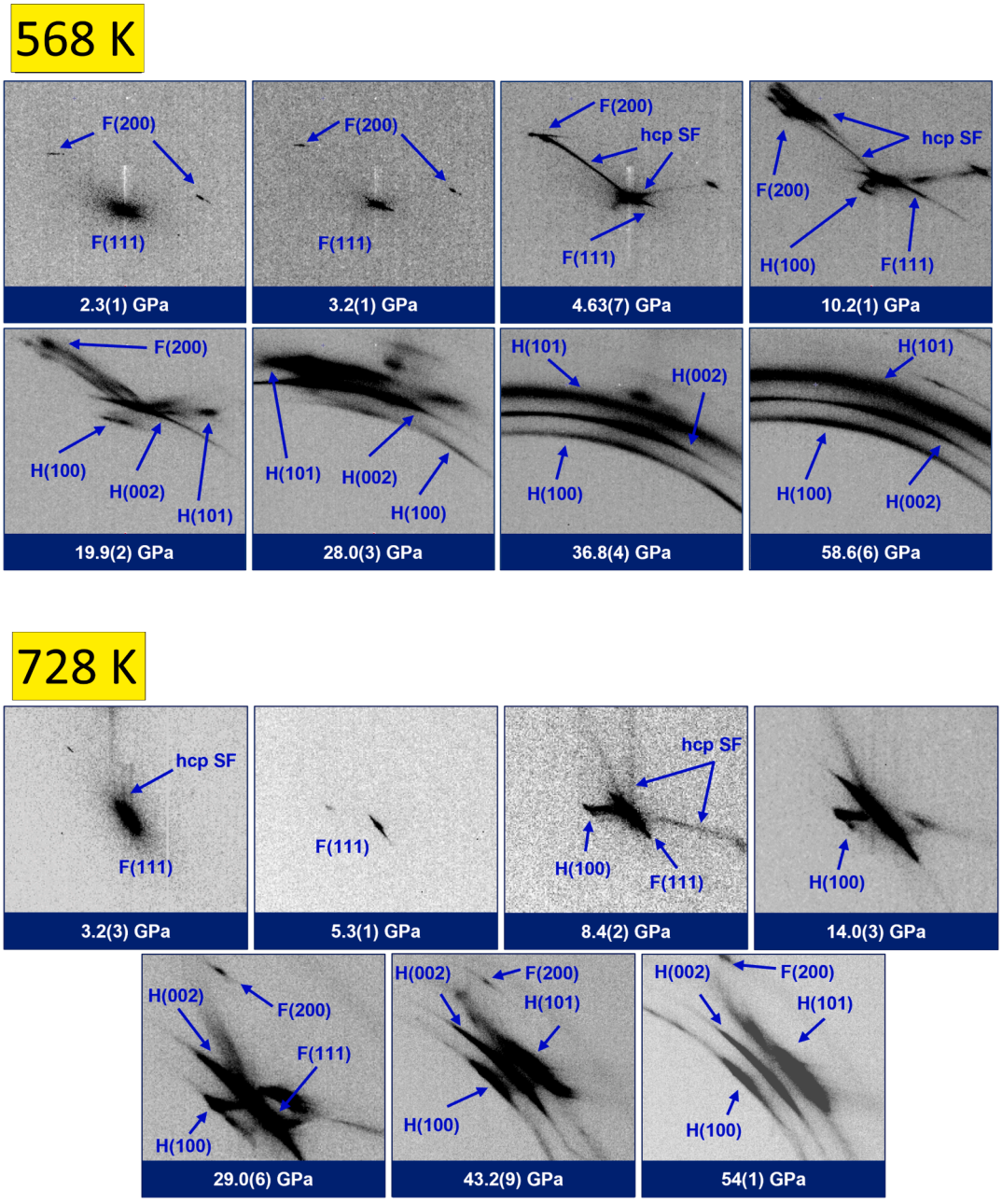

Fig. 1. Pressure Evolution of the raw diffraction images taken in the vicinity of the fcc(1 1 1) Bragg reflection for run 2 at 568 K and run 3 at 728 K. Bragg reflections assigned to the fcc and hcp phases are indexed with (*h k l*) values and denoted with a capital F or H, respectively. The pressure at which each figures was taken is given below the figure and in parenthesis the uncertainty is given.

et al. (2015). In brief, the X-ray beam energy was monochromatized and scanned using a fixed exit double-crystal monochromator equipped with a pair of Si(3 1 1) crystals. Two Pt-coated mirrors were employed for beam focusing and high harmonics rejection. Ion chambers filled with optimized gas mixtures of He and Kr to achieve high X-ray beam absorption of 30 % and 70 %, respectively, were placed before and after the sample to accurately determine the incoming and transmitted beam intensities. X-ray Absorption Near Edge Structure (XANES) and Extended X-ray Absorption Fine Structure (EXAFS) data were acquired across the melting curve of xenon at pressures ranging from 0.1 to 3.5 GPa and temperatures from 393 to 623 K. The raw data were analysed using the Demeter software package (Ravel and Newville, 2005). As presented in Figure S4 and S5, upon crystallization and melting of xenon, clear changes in the XANES features were observed and have been used to determine the melting line of xenon. The extracted EXAFS functions $\chi(k)$ of liquid and solid xenon show low amplitudes of maxima and minima ($\Delta k^2\chi(k) < 0.2$ Å^{-2}). In addition, the EXAFS signal exhibits a fast damping at *k*-values beyond 6 Å^{-1} (Figure S4, right). The EXAFS data were used to cross-check the thermo-elastic parameters obtained in the XRD runs using full multiple scattering computations. They were also employed to establish the vibrational properties of xenon from the pressure-evolution of the bond distance variations by combining the present data with those obtained in our previous works (Rosa et al., 2022).

3. Results and discussion

3.1. Diffraction data of xenon

As an example, a series of integrated XRD patterns collected along

the isothermal pathway at 568 K is shown in Fig. 2. The pressure evolution of the refined hcp volume fraction is presented in the supplementary Figure S6. In the investigated temperature range, no evidence for a systematic effect of temperature on the kinetics of the martensitic transformation was found. In all runs, a residual amount of the fcc phase was observed up to the highest achieved pressures (55–60 GPa) confirming that the transformation was not compete. This observation is in agreement with previous works that reported a completion of the transformation at pressures in excess of 70(±5) GPa independently of the temperature annealing history of the sample (Cynn et al., 2001; Rosa et al., 2022) Fig. 5). The pressure evolution of the crystal domain size of the fcc (CDS_{FCC}) and hcp (CDS_{HCP}) phase of runs 1–3 are shown in Figure S7. For both phases, the CDSs follow the expected trend for a martensitic transformation as reported in Rosa et al. (2022).

The volumes and lattice parameters extracted from the XRD patterns of fcc and hcp xenon by Rietveld refinement are listed in Table 2. The accuracy of the atomic lattice volumes determination ranges between 0.005 and 0.08 $Å^3$ for both the fcc and hcp phase. Higher uncertainties are found at low-pressure conditions due to peak broadening effects and, when the volume fractions of the phases are low. The evolution of the unit cell volumes for the three high-T runs and that reported under ambient conditions for both fcc and hcp xenon are shown in the supplementary Figure S8. The temperature variation of the thermal expansion of FCC xenon is clearly visible at pressures below 10 GPa (inlet of Figure S8). Above this pressure, the effect of pressure on the compressibility dominates, leading to the overlapping (within uncertainties) of the isothermal volume compression curves for runs 1–3. The response of V_{hcp} xenon to increasing temperature is less pronounced than that of the fcc phase (Figure S8 right). At low pressure (<20 GPa), the thermal expansion of hcp xenon only slightly dominates the volume compression term, resulting in minor increases of V_{hcp} values for the three isothermal runs. At higher pressures, the isothermal compression curves overlap within their uncertainties.

The pressure evolution of the c/a ratio of hcp xenon is presented in Table 2 for runs 2–3. In run 2 (568 K isotherm) hcp iron exhibits an c/a ratio close to the ideal one of 1.633. In contrast, in run 3 (728 K isotherm), the obtained c/a ratios were systematically greater than the ideal value reaching up to 1.644. This could suggest that above 728 K the hcp xenon is more compressible along the a-axis or thermally expands more along the c-axis. This would also imply a variation of the elastic anisotropy with increasing pressure. A similar behaviour has been experimentally observed and theoretically predicted for the ε phase of

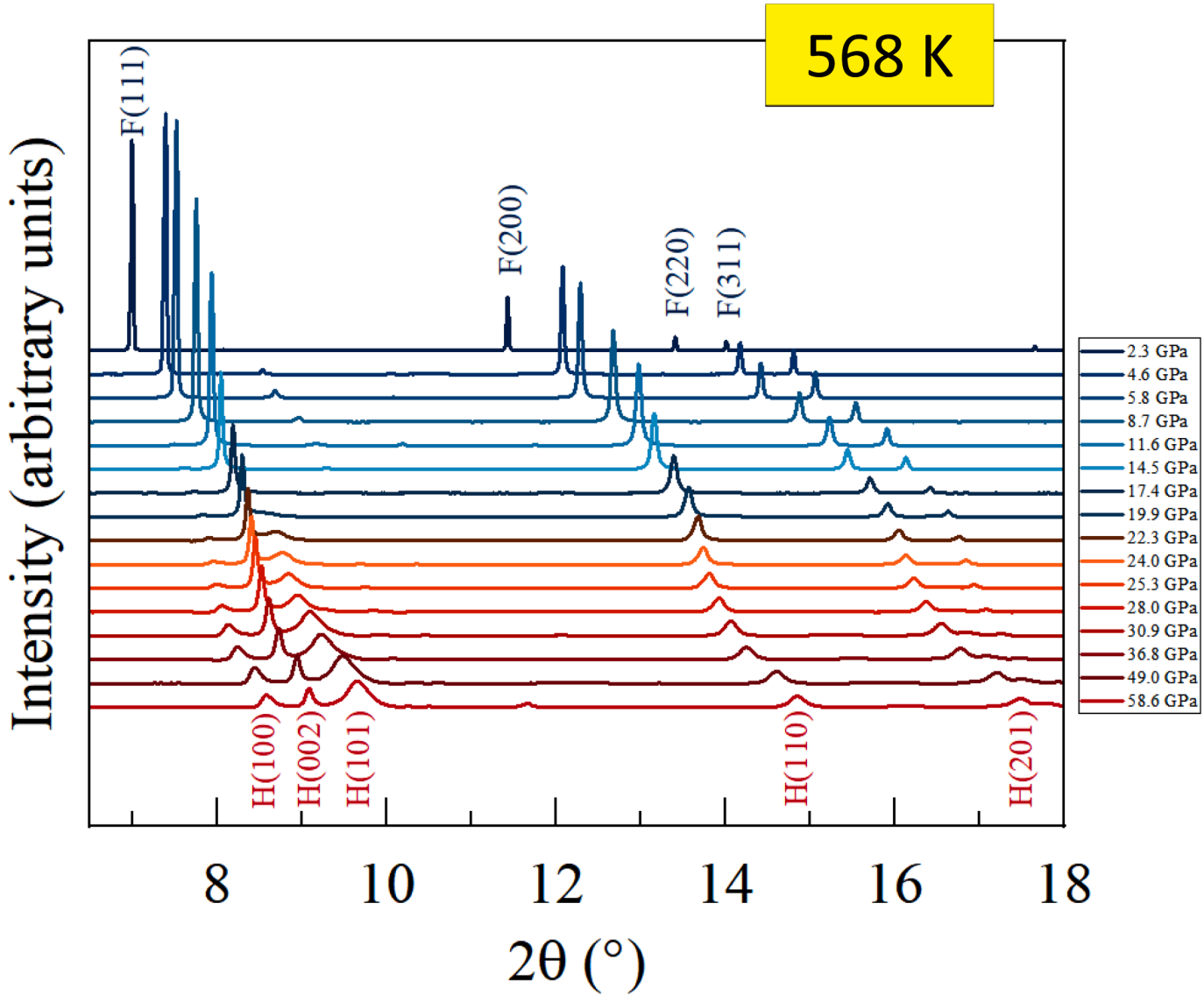

Fig. 2. Pressure evolution of the integrated XRD patterns collected at the centre of the sample along the 568 K isotherm (run 2). The Bragg reflections assigned to the fcc and hcp phase are denoted with capital letters F and H, respectively.

Table 2
Crystallographic parameters of fcc and hcp xenon extracted from Rietveld refinement from diffraction images taken at the gold position. Given uncertainties result from the least square refinement of the data. The parameters below were used to determine the thermal equation of state parameters of xenon.

	Pressure (GPa)	V_{au} (Å^3)	$V_{(at)\ fcc}$ (Å^3)	$V_{(at)\ hcp}$ (Å^3)	c/a	VF_{hcp} (%)
Run 1 429 K						
1	1.39(14)	67.839(1)	54.48(7)			
2	1.42(14)	67.831(1)	53.78(8)			
3	1.43(14)	67.827(1)	53.38(6)			
4	1.47(15)	67.812(1)	52.86(2)			
5	1.52(15)	67.788(2)	52.366(6)			
6	1.54(15)	67.781(2)	52.169(5)			
7	1.58(16)	67.766(3)	51.845(9)			
8	1.60(16)	67.755(2)	51.48(1)			
9	1.72(17)	67.708(2)	50.652(7)			
10	1.94(19)	67.619(1)	49.510(8)			
11	1.98(20)	67.604(1)	49.393(9)			
12	2.00(20)	67.596(2)	49.23(1)			
13	2.3(2)	67.4860 (8)	47.94(1)			
14	2.4(2)	67.4480 (9)	47.508(5)			
15	2.6(3)	67.376(1)	46.872(3)			
16	2.7(3)	67.3192 (9)	46.247(4)			
17	3.0(3)	67.2190 (9)	45.387(5)			
18	3.2(3)	67.125(1)	44.630(5)			
19	3.7(3)	66.932(1)	43.416(6)			
20	3.9(2)	66.849(1)	42.826(9)			
21	4.3(2)	66.694(1)	42.121(6)			
22	4.6(1)	66.596(1)	41.63(8)			
23	5.1(1)	66.430(1)	40.91(1)			
24	5.4(1)	66.320(1)	40.45(1)			
25	5.6(1)	66.256(2)	40.05(1)			
26	5.8(1)	66.158(3)	39.64(1)			
27	6.0(1)	66.097(1)	39.42(1)			
28	6.1(1)	66.064(2)	39.25(1)			
29	6.2(1)	66.031(1)	39.09(1)			
30	6.6(1)	65.881(2)	38.50(2)			
31	6.9(1)	65.803(2)	38.18(2)			
32	7.2(1)	65.698(2)	37.82(2)			
33	7.5(1)	65.603(2)	37.49(2)			
34	7.8(2)	65.489(2)	37.12(2)			
Run 2 568 K						
1	2.31(17)	67.8871 (7)	49.734(9)			
2	2.32(18)	67.8846 (7)	49.702(9)			
3	2.38(21)	67.8600 (9)	49.344(3)			
4	2.39(21)	67.8553 (9)	49.279(3)			
5	2.43(25)	67.838(1)	49.066(3)			
6	2.58(30)	67.775(2)	48.373(3)			
7	2.61(32)	67.764(1)	48.267(2)			
8	2.68(38)	67.735(2)	48.068(2)			
9	2.74(45)	67.710(2)	47.750(2)			
10	2.81(43)	67.683(2)	47.354(2)			
11	3.2(3)	67.519(3)	46.248(2)			
12	3.5(3)	67.416(2)	45.462(2)			
13	3.59(28)	67.369(2)	45.105(2)			
14	3.58(43)	67.370(1)	45.015(3)			
15	3.7(2)	67.330(1)	44.754(2)			
16	3.8(2)	67.276(1)	44.320(2)			
17	4.6(1)	66.964(1)	42.298(2)			
18	5.3(1)	66.697(1)	40.954(2)			0.07
19	5.8(1)	66.536(2)	40.202(2)			0.18
20	6.7(1)	66.213(1)	38.967(2)	38.699(5)		0.17
21	7.4(1)	65.959(1)	38.047(2)	37.761(4)		0.24
22	8.7(2)	65.533(1)	36.691(2)	36.323(4)		0.29
23	9.6(2)	65.234(1)	35.915(1)	35.576(3)		0.61
24	10.2(2)	65.024(2)	35.344(2)	34.969(2)		0.69
25	11.6(2)	64.601(2)	34.334(2)	33.972(2)		0.68
26	13.9(3)	63.925(2)	32.953(2)	32.580(3)		0.6
27	14.2(3)	63.838(2)	32.776(2)	32.336(3)		0.63
28	14.5(3)	63.761(2)	32.640(2)	32.366(2)		0.69
29	15.2(3)	63.577(2)	32.259(2)	31.983(2)		0.73
30	15.7(3)	63.437(2)	32.006(2)	31.824(1)		0.82
31	16.2(3)	63.299(3)	31.734(3)	31.552(2)		0.85
32	17.4(3)	62.979(3)	31.076(3)	31.349(6)		0.81
33	18.5(4)	62.700(2)	30.646(2)	30.229(3)		0.78
34	19.9(4)	62.351(3)	30.071(3)	30.038(6)		0.76
35	22.3(4)	61.770(2)	29.220(3)	29.241(2)	1.632	0.8
36	23.2(5)	61.581(3)	29.004(4)	29.007(4)	1.632	0.8
37	23.9(5)	61.410(4)	28.760(9)	28.718(3)	1.633	0.74
38	24.4(5)	61.301(4)	28.65(1)	28.625(4)	1.632	0.8
39	25.3(5)	61.111(5)	28.418(5)	28.361(6)	1.634	0.64
40	26.6(5)	60.834(5)	28.090(5)	28.054(5)	1.634	0.77
41	28.0(6)	60.545(6)	27.728(6)	27.666(3)	1.632	0.8
42	29.0(6)	60.336(5)	27.430(5)	27.383(4)	1.631	0.87
43	29.7(6)	60.20(1)	27.10(1)	27.019(4)	1.633	0.89
44	30.7(6)	60.001(4)	26.741(4)	26.681(3)	1.631	0.88
45	30.9(6)	59.964(5)	26.672(5)	26.612(5)	1.629	0.89
46	32.7(7)	59.628(2)	26.430(2)	26.417(6)	1.633	0.89
47	33.4(7)	59.495(3)	26.324(3)	26.242(6)	1.630	0.89
48	34.5(7)	59.289(2)	26.157(2)	26.152(4)	1.633	0.89
49	36.8(7)	58.880(2)	25.749(2)	25.669(4)	1.629	0.89
50	39.3(8)	58.451(2)	25.263(2)	25.221(3)	1.633	0.9
51	41.4(8)	58.107(2)	24.946(2)	24.919(3)	1.632	0.9
52	44.0(9)	57.694(2)	24.580(2)	24.527(4)	1.633	0.9
53	44.7(9)	57.589(2)	24.462(2)	24.385(5)	1.632	0.9
54	45.4(9)	57.476(2)	24.319(2)	24.214(5)	1.632	0.9
55	47.3(9)	57.202(2)	24.142(2)	24.089(5)	1.632	0.9
56	49(1)	56.952(2)	23.881(2)	23.809(4)	1.632	0.9
57	51(1)	56.672(2)	23.650(2)	23.565(3)	1.633	0.9
58	52(1)	56.511(2)	23.467(2)	23.432(3)	1.633	0.91
59	53(1)	56.374(2)	23.381(2)	23.318(5)	1.632	0.93
60	54(1)	56.214(2)	23.280(2)	23.165(4)	1.630	0.92
61	56(1)	56.033(4)	23.077(4)	23.001(4)	1.630	0.91
62	58(1)	55.793(2)	22.915(2)	22.851(5)	1.632	0.9
63	59(1)	55.651(2)	22.765(2)	22.724(4)	1.632	0.86
Run 3 728 K						
1	3.22(13)	68.016(1)	47.189(4)			
2	3.24(12)	68.008(2)	47.034(5)			
3	3.42(14)	67.934(1)	46.489(3)			
4	3.5(1)	67.891(1)	46.083(4)			
5	3.77(9)	67.783(1)	45.353(3)			
6	4.06(8)	67.663(1)	44.593(4)			
7	4.38(7)	67.534(1)	43.809(3)			
8	4.72(5)	67.398(1)	42.835(3)			
9	5.56(6)	67.064(1)	41.252(2)			
10	6.03(6)	66.884(1)	40.477(3)			
11	6.29(6)	66.782(1)	40.048(2)			
12	6.58(7)	66.674(1)	39.591(3)			
13	7.62(8)	66.2941 (9)	38.251(3)			
14	8.38(8)	66.0221 (8)	37.412(3)			
15	8.50(9)	65.9791 (8)	37.257(3)			
16	9.6(1)	65.5945 (8)	36.145(3)			0.3
17	10.5(1)	65.3120 (8)	35.429(3)			0.38
18	12.5(1)	64.6664 (6)	33.897(3)			0.39
19	12.8(1)	64.5762 (7)	33.740(3)			0.39
20	13.2(1)	64.4509 (7)	33.475(3)			0.33
21	14.0(1)	64.2278 (7)	33.037(3)	32.688(3)	1.635	0.22
22	15.1(2)	63.8901 (7)	32.397(4)	32.246(4)	1.635	0.21

(*continued on next page*)

Table 2 (*continued*)

	Pressure (GPa)	V_{au} (Å^3)	$V_{(at)\ fcc}$ (Å^3)	$V_{(at)\ hcp}$ (Å^3)	c/a	VF_{hcp} (%)
23	15.7(2)	63.7352 (8)	32.120(4)	31.958(3)	1.637	0.17
24	17.6(2)	63.2128 (8)	31.266(4)	31.081(3)	1.636	0.17
25	18.8(2)	62.8842 (9)	30.751(4)	30.543(3)	1.634	0.18
26	20.9(2)	62.352(1)	29.956(5)	29.751(3)	1.635	0.19
27	22.0(2)	62.0874 (9)	29.488(5)	29.360(3)	1.635	0.22
28	23.0(2)	61.8663 (9)	29.214(5)	29.015(4)	1.637	0.24
29	24.3(2)	61.5600 (9)	28.769(5)	28.522(4)	1.639	0.28
30	26.9(3)	60.9823 (9)	27.960(5)	27.839(6)	1.640	0.35
31	28.2(3)	60.7081 (9)	27.707(6)	27.494(5)	1.639	0.34
32	29.3(3)	60.4704 (9)	27.490(6)	27.237(3)	1.638	0.31
33	31.2(3)	60.086(1)	27.018(7)	26.720(5)	1.641	0.36
34	33.5(3)	59.659(1)	26.516(5)	26.239(3)	1.641	0.48
35	34.0(3)	59.5570 (9)	26.377(5)	26.069(3)	1.643	0.43
36	35.4(4)	59.2927 (9)	26.100(5)	25.760(3)	1.640	0.45
37	37.7(4)	58.8930 (9)	25.625(5)	25.397(3)	1.644	0.75
38	39.8(4)	58.5193 (9)	25.265(4)	24.920(2)	1.641	0.68
39	43.2(4)	57.9694 (9)	24.722(5)	24.487(3)	1.639	0.77
40	44.4(4)	57.7764 (8)	24.554(5)	24.332(2)	1.640	0.69
41	47.0(5)	57.3823 (7)	24.027(6)	23.823(3)	1.634	0.72
42	47.9(5)	57.2475 (7)	23.830(5)	23.644(4)	1.635	0.72
43	49.3(5)	57.0380 (6)	23.539(5)	23.321(3)	1.637	0.75
44	51.6(5)	56.7091 (6)	23.376(5)	23.157(3)	1.636	0.8
45	53.0(5)	56.5103 (6)	23.308(5)	23.091(2)	1.636	0.8
46	53.6(5)	56.4186 (7)	32.397(6)	32.246(2)	1.635	0.89

iron (Mao et al., 1990; Steinle-Neumann et al., 2001; Ma et al., 2004; Gannarelli et al., 2005) with important implication for the expected elastic anisotropy of the Earth's core. Data on xenon at higher temperatures are needed to confirm this behavior and draw conclusions about how its elastic anisotropy changes with temperature.

3.2. Thermal equation of state of solid xenon

The pressure–volume data of fcc xenon from runs 1–3 and those reported from ambient conditions (Rosa et al., 2022) were adjusted to a thermal equation of state (EOS). The effect of temperature on the lattice volume of fcc xenon is significant for pressures below 10 GPa (Table 2 and Fig. 3), while at higher pressures this effect is negligible. We did not fit a thermal EOS to the hcp data because hcp xenon stabilizes at higher pressures and, due to the absence of a measurable variation of the hcp lattice volume within the probed temperature range.

For fitting the pressure–temperature-volume data of fcc xenon a Birch-Murnaghan (BM) EOS integrating the Mie-Grueneisen-Debye thermal term (MGD) was employed for fitting the fcc xenon using the program EOSfit (Gonzalez-Platas et al., 2016). In this formalism, the pressure in solid fcc xenon is expressed as a sum of static pressures $P_0(V)$ at 0 K (using the BM EOS, with V_0 the volume at ambient pressure and 0 K) and a thermal pressure $P_{th}(V, T)$ estimated from the quasi-harmonic MGD model:

$$P(V,T) = P_0(V) + P_{th}(V,T):$$

$$\mathrm{P(V)} = \frac{3K_0}{2}\left[\left(\frac{V_0}{V}\right)^{\frac{7}{3}} - \left(\frac{V_0}{V}\right)^{\frac{5}{3}}\right]\left\{1 + \frac{3}{4}(K_0' - 4)\left[\left(\frac{V_0}{V}\right)^{\frac{2}{3}} - 1\right]\right\}$$

and

$$P_{th}(V,T) = \frac{3\gamma RT}{V}\left[D\left(\frac{\theta_D}{T}\right)\right]$$

where K_{T0} is the bulk modulus, K' its pressure derivative and V_0 the equilibrium molar volume, D the Debye function, θ_D the Debye temperature and γ the Grüneisen parameter ($\gamma(V) = \gamma_0 \left(\frac{V}{V_0}\right)^q$) with $\theta = \theta_D exp\left(\frac{\gamma_0 - \gamma(V)}{q}\right)$. Because of the strong correlation between θ_D, q and γ_0, we used a q-dependant model with $q = 1$ in which the ratio γ/V is

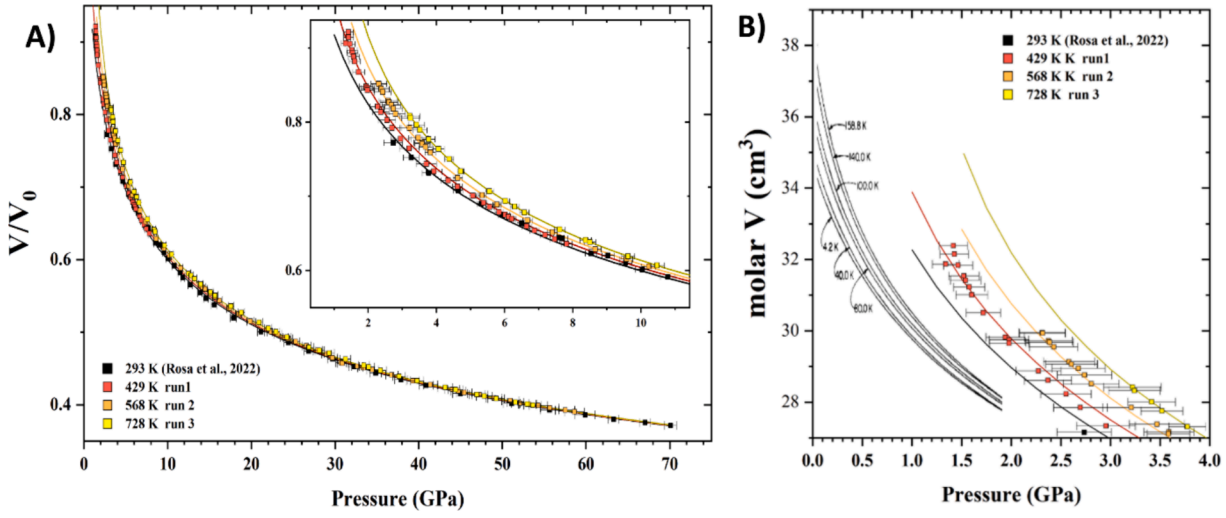

Fig. 3. Left panel: Experimental and fitted reduced volume data for fcc xenon and its evolution with pressure. The experimentally obtained molar volumes were normalized to the molar volume of 35.155 cm^3/mol obtained from fitting (Table 2). Uncertainties on the pressure values are shown, uncertainties on normalized volumes are smaller than the symbol size. Right panel: Comparison of the molar volume data of fcc xenon of this study and those reported by Anderson and Swenson (1975).

assumed to be constant. The adjusted parameters were K_{T0}, K', V_0 and γ_0. θ_D was fixed to 64(1) K as reported by Fenichel and Serin (1966). The fitted reduced volume curves to the present data are shown in Fig. 3 and the results of the adjustments are presented and compared to previous literature data in Table 3.

The fitted reference volume V_0 of fcc xenon at 0 K is in close agreement with those reported in recent works (Dewaele et al., (2012) and Rosa et al. (2022)) but is higher than that obtained by Anderson and Swenson (1975). This discrepancy may be related to differences in volume determination methodologies. Anderson and Swenson (1975) have used indirect volume measurements while in the present work synchrotron XRD was employed to directly determine the lattice volumes. We also obtained a slightly higher γ value than that obtained by Anderson and Swenson (1975).

3.3. Lattice vibrations at low pressure

Knowledge of the evolution of the vibrational properties of zero-charged Xe is key to understand its incorporation mechanism in vacancies of host structures and its diffusive properties (Wang et al., 2020) or the bonding character of noble-gas compounds (Khriachtchev et al., 2000; Miao et al., 2015). The present XRD and XAS data obtained at low pressure (<3 GPa) reveal significant contributions of thermal vibrations in solid Xe. These are manifested in the strong broadening of single-crystalline peaks (Fig. 1) and in the weak and short EXAFS signal (Figure S4). These observations reflect the weak interatomic van der Waals interactions at these conditions. With increasing pressure, these vibrations are progressively suppressed leading to sharp XRD peaks as well as longer-range EXAFS signals for pressures above 3 GPa (Rosa et al., 2022). Similarly to Xe, in Ne the occurrence of thermal vibrations and their suppression with pressure have been experimentally evidenced and theoretically explained (see references in Dewaele et al. (2008)). The Debye temperature Θ_D is related to the interatomic bond strength while the Grueneisen-parameter γ provides information on the evolution of Θ_D with temperature and/or pressure. Xenon exhibits the lowest Θ_D among the noble gases (Jephcoat, 1998) while the high γ value obtained in this work indicates a fast increase of Θ_D with pressure. The EXAFS data were used to verify the fitted thermal EOS parameters by comparing our experimental data to those calculated using a self-consistent FEFF modelling. For these calculations, the structure and lattice parameter of fcc xenon at ambient conditions (a = 6.172 Å) and the Debye model (using the Debye temperature at 0 K taken from (Fenichel and Serin (1966)) were employed as input parameters.

The computational results are presented in Fig. 4 and clearly demonstrate that the EXAFS function is very weak for Xe and quickly levels off beyond $k = 6$ under ambient P-T conditions. This theoretical result is in good agreement with experiments (Fig. 4 and S4 of the supplementary material) and confirms the weakly bonded nature of Xe in the liquid and solid state that is dominated by van der Waals forces in the low P/T domain up to 3 GPa and 728 K probed by XAS in this study. Further calculations that we conducted at 0 K revealed that the EXAFS function amplitude increases significantly and the signal extends to high k-values (beyond 20 Å^{-1}). A similar effect was experimentally observed using XAS at elevated pressures (>3 GPa and up to 150 GPa) and room temperature (Rosa et al., 2022). This behaviour may originate from to the rapid increase of the Debye term due to the high γ value that leads to the strong reduction of the thermal vibrations for both cases. This suggests that weak EXAFS signals could be separated from the low instrumental noise. This confirms the accuracy of the reported Debye terms employed in the EOS fits. The calculations further suggest that the incorporation of Xe atoms in host lattice vacancies that are slightly smaller than their zero-charged radii could lead to the compression of its atomic volume and to the reduction of the thermal vibrations. Such a mechanism would hinder diffusional loss of Xe and favour its retention.

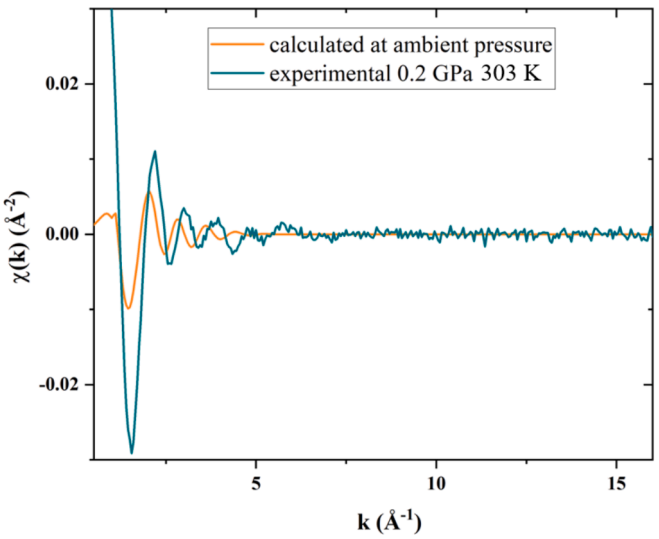

Fig. 4. Comparison between the experimentally obtained and the theoretical EXAFS functions of xenon (blue and orange curves, respectively). The theoretical EXAFS function was calculated using the thermal EOS terms obtained in this study and full multiple self-consistent calculations (FEFF). Note, the small calculated amplitude in the calculated EXAFS function that corresponds closely the experimental one. Note, that the slightly higher amplitude of the experimental EXAFS function and the shift of the EXAFS oscillations to higher k-values is related to elevated pressures and the high compressibility of xenon.

Table 3
Thermal and ambient temperature EOS data of fcc xenon obtained in this work and reported from in literature. BM, M and GMD correspond to Birch-Murnaghan, Murnaghan and Mie-Grüneisen-Debye model, respectively. V_0, K0, K′, Θ_D and γ correspond to the molar volume, the bulk modulus, its pressure derivative, the Debye temperature and the Grüneisen-parameter at 0 K, respectively. Discrepancies in reported EOS parameters from studies that conducted only high pressure measurements at ambient temperature are mainly related to the fcc-hcp martensitic transition as discussed in Rosa et al. (2022).

Reference	Method	Model	V_0 (cm^3/mol) at 0 K	K_0 (GPa)	K′	Θ_D (K)	γ
This work	XRD 60 GPa, 728 K	BM Mie-MGD	35.2 (3)	4.48(2)	5.58(2)	64(1)*	3.2(1)
Jephcoat (1998)	XRD High P/T exact values are not given	Mie-MGD	34.74+	6.5(1)	4.3(2)	57	2.36
Anderson and Swenson (1975)	Indirect method to 4 K, 2 GPa	M Mie-MGD	34.74	3.65(7)	7.09(3)	55	2.9
Asaumi (1984)	XRD 32 GPa	BM Mie-MGD	34.74+	5.2(3)	5.5(2)	64(1)*	2.9+
Rosa et al. (2022)	XRD to 75 GPa (stability limit of the fcc phase)	Vinet	35.4(1)	4.54	6.26(1)		
Dewaele et al. (2012)		Rydberg-Vinet	35.19	4.887	6.18		
Cynn et al. (2001)		3rd order BM	37.94	3.6(5)	5.5(4)		

$corresponds to γ_1 in the formula $\gamma = \gamma_1(V/V_0 + 0.5)$.
* fixed to the one reported in Fenichel and Serin (1966).
+ fixed to the one reported in Anderson and Swenson (1975).

4. Geophysical implications

4.1. Assessment of noble gas solubilities at extreme conditions

The determination of noble gas solubilities at extreme conditions in melts and minerals remains a major challenge and, only few experimental and theoretical studies have been dedicated to this subject (Lancet and Anders, 1973; Zaikowski and Schaeffer, 1979; Chamorro et al., 2002; Brooker et al., 2003; Bouhifd and Jephcoat, 2006; Heber et al., 2007a; Shcheka and Keppler, 2012; Jackson et al., 2013; Jackson et al., 2015; Krantz et al., 2019; Bouhifd et al., 2020; Rosa et al., 2020; Jackson et al., 2021). This is mainly related to the very high dilution levels of noble gases that are challenging to investigate both theoretically and experimentally. Another problematic for experimental solubility studies are the peculiar properties of noble gases including their very weak bonding character and large pressure response. These properties may lead to the redistribution or loss of noble gases after pressure–temperature quenching to ambient conditions. In addition, similarly to natural samples, any signal contamination from air or gas bubbles in the recovered samples must be identified and carefully excluded in the analysis. Due to these challenges, significant disagreements have emerged between experimentally determined solubilities and those extracted from natural samples (Chamorro et al., 2002; Moreira and Raquin, 2007; Roubinet and Moreira, 2018). Major breakthroughs in the study of noble gas concentrations in natural and synthetic samples recovered from extreme pressure–temperature conditions have been achieved thanks to the use of micro analytical methods. These includes micrometric lasers to study gas vesical in glasses or electron probe analysis methods (EMPA UVLAMP) (Raquin et al., 2008). These methods have been combined to lattice strain modelling and/or atomistic simulations (Brooker et al., 2003; Heber et al., 2007b) to establish clear relations between noble gas radii and solubilities in structural units of amorphous or crystalline materials. This methodology is the basis of this work, the main object of which is to determine precisely the variation of the noble gas radii as a function of pressure and temperature and to employ lattice strain modelling to obtain noble gas solubilities in hydrous minerals. As we have previously shown (Rosa et al., 2020), for such models, not only the mechanical properties of the noble gases are of central importance, but also those of the host structure and, more specifically, those of the structural incorporation site. For instance, the observed solubility drop of noble gases in silicate melts at 15 GPa has been related to the densification of the melt structure associated to the loss of void spaces due to the increase of coordination of the Si-O polyhedra from 4 to 6-fold (Bouhifd and Jephcoat, 2006; Krstulović et al., 2022).

4.2. Lattice strain modelling (LSM)

Precise knowledge of the radii size of zero-charged pure noble gases is essential for inferring their solubilities in minerals and melts at high *P/T* conditions and, therefore, predict their geochemical behaviour in the deep Earth's interior (Shcheka and Keppler, 2012; Crepisson et al., 2018a; Crepisson et al., 2018b; Wang et al., 2020; Rosa et al., 2022). As presented in Table 3, the compressibility of pure noble gases is very large at ambient temperature and further increases with their atomic number. For instance, the atomic volumes of argon and xenon reduce by more than 47 % and 58 % at 20 GPa, respectively (Dewaele et al., 2021; Rosa et al., 2022). In previous experimental studies devoted to the solubility of noble gases in lower Earth's mantle phases (Rosa et al., 2020), it was suggested that this effect may explain their increasing compatibilities in mineral phases. In contrast, and with the exception of the low-pressure regime (P < 3 GPa), the temperature response is much weaker. Indeed, the present data clearly show that the thermal expansion term dominates only at low pressures (Table 3) and reduces greatly with increasing atomic number (Jephcoat, 1998; Dewaele et al., 2008). In addition, as shown for Xe, due to the weak interatomic van der Waals interactions, the thermal vibrations of noble gases atoms within a neutral crystalline lattice at hydrothermal conditions are very strong. This suggests that light noble gases exhibit larger diffusive potentials at low pressures than heavy noble gases and, that for all noble gases this effect is progressively suppressed at higher pressures.

The incorporation mechanism of noble gases into hydrous minerals such as antigorite is not fully clarified. A strong relation between the absolute solubilities of light noble gases (He, Ne, Ar) and the open host structure formed of six-membered rings made of silicon tetrahedra for a set of hydrous minerals has been reported by Jackson et al. (2015). This provided a strong argument for a scenario in which the light noble gases are incorporated into these vacancy sites. However, experimental evidence for this incorporation mechanism is presently lacking. In this work, modelling based on the lattice strain theory have been conducted to test the most likely host sites for noble gases in antigorite. These models also aim to better understand reported discrepancies in noble gases elemental solubility models from field and experimental studies (Jackson et al., 2015; Krantz et al., 2019).

Lattice strain modeling (LSM) is a well-established empirical approach in experimental geochemistry that relates the solubility of trace elements, including noble gases, with their compatibility in a specific host site (Blundy and Wood, 2003; Brooker et al., 2003; Heber et al., 2007a; Shcheka and Keppler, 2012). In practice, the empirical equation developed by Blundy and Wood (2003) was employed to extract the solubility of the noble gas (c_i) from the (effective) host site stiffness *Em* and the radii difference between the zero-charged noble gas atom and that of neutral vacancy site (r_i-r_0):

$$c_i = c_0 \times exp\left\{\frac{-4\pi N_A E_m\left[\frac{1}{2}r_0(r_i - r_0)^2 + \frac{1}{3}(r_i - r_0)^3\right]}{RT}\right\}$$

where N_A is the Avogadro's number and R the gas constant. The maximal solubility of the host site c_0 is an adjusted parameter. E_m is obtained using the relation: $E_m = (9 * K * G)/(3 * K + G)$, where K and G are the bulk and shear modulus, respectively.

An extended form of the LSM that takes into consideration the thermo-elastic data of the trace elements (noble gases) and the host phase was employed following the method detailed in Rosa et al. (2020) (see Supplementary Information therein). In this approach, the significant effect of coordination change on noble gas radii that could result in radii differences of up to 0.3 Å was considered (Zhang and Xu (1995)). As shown in Rosa et al. (2020), this approach reproduces well the measured solubility patterns of noble gases at Earth's lower mantle conditions.

As a first step, the atomic radii variation of the set of noble gases as a function of the coordination number and along subduction zone geotherms have been obtained using the thermal EOS parameters listed in Table 4. In a second step, the strain energy generated by a zero-charged noble gas atom with a radius r_i that is incorporated in a neutral crystal lattice vacancy site with radius r_0 was determined. To this aim, the

Table 4
Thermo-elastic parameters for noble gases based on the Mie-Grüneisen formalism used to calculate their radii at high *P/T* conditions.

	V_0 (cm^3/mol)	K_0 (GPa)	K′	Θ_D (K)	γ_0	Q
Ar[a]	22.885	2.65	7.42	93.3	2.7	$\gamma = 2.20*(V/V_0) + 0.5$
Kr[b]	27.094	3.32	7.23	71.9	2.8[d]	1
Xe[c]	35.16	4.48(2)	5.58(2)	64(1) [d]	3.2(1)	1

[a] Parameters taken from Dewaele et al. (2021).
[b] Parameters taken from Jephcoat (1998).
[c] Parameters taken from this work.
[d] Taken from Anderson and Swenson (1975).

average radii of potential host vacancy sites in antigorite were calculated using the ambient conditions lattice parameters and the thermal equation of state of antigorite reported in Capitani and Mellini (2006) and Yang et al. (2014), respectively. The averaged distances between opposed atoms was employed to establish the radii of neutral sites.

The principal incorporation site in antigorite is the charge-neutral void space between the six membered rings of SiO_4 tetrahedra. It has a coordination number of 10 (6 oxygen and 4 hydrogen atoms) and a radius of 2.54 Å at ambient conditions. Secondary, less probable, neutral host sites are the vacant MgO_6 octahedra (2.1 Å atomic radius). Such neutral vacancies, known as the tri- to di-octahedral substitution, are frequently generated in phyllosilicates *via* the substitution of two trivalent cations such as Fe^{3+} or Al^{3+} for two divalent Mg^{2+} cations. Neutral tetrahedral vacancy sites with atomic radius of 1.62 Å that form as neutral Schottky pair defect clusters are less probable in antigorite. For Schottky defects, ions with opposite charge are absent in the structure to ensure charge neutrality of the bulk structure. Such defects can occur on the octahedral or tetrahedral sites, but would exhibit very low defect densities. For each potential incorporation site, the atomic radii differences (r_i-r_0) between the host sites and the noble gases was calculated. As a first approximation, for all incorporation sites, the effective Young's modulus (E_m) for antigorite was determined using the thermo-elastic data reported by Reynard et al. (2007).

4.3. *Incorporation mechanism at hydrothermal conditions (<0.1 GPa and < 623 K)*

Calculated solubility (Henry's constants at 1 bar) curves for different host sites and noble gas radii as a function of coordination environment using LSM are shown in Fig. 5. They are compared to the experimental data acquired at 0.1 GPa and 623 K for constant partial noble gas pressure (Jackson et al., 2015; Krantz et al., 2019). At this low pressure, the ambient condition noble gas radii reported by Zhang and Xu (1995) have been used. They are the most relevant ones, as at these *P-T* conditions noble gases are in a supercritical state and composed of isolated uncompressed atoms.

As presented in Fig. 5a and b, the observed solubility patterns for heavy noble gases with the relation $c_{Ar} < c_{Kr} < c_{Xe}$ can be best reproduced for the six membered rings composed of SiO_4 tetrahedra or octahedral vacancies. Indeed, the radii of Ar, Kr and Xe in 6 and 10-fold

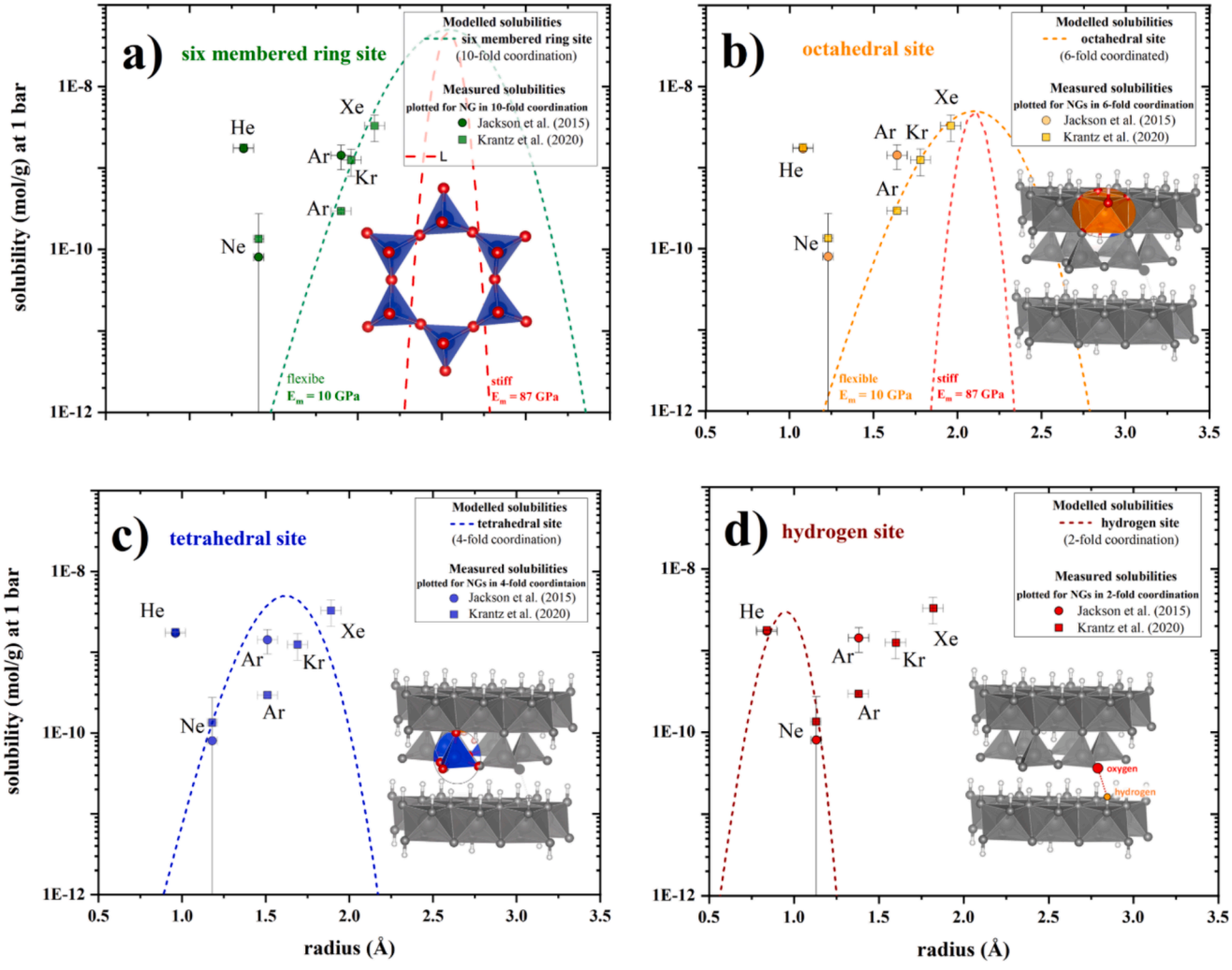

Fig. 5. a-d) solubility trends (henry's constants at 1 bar) at 0.1 GPa and 623 K as a function of the noble gas radius obtained from LSM for different vacancy sites that include **a)** six-membered SiO_4 rings (green dashed line), **b)** octahedral sites (orange dashed line), **c)** tetrahedral sites (blue dashed line) and **d)** the hydrogen Van der Waals bond site (red dashed line). Noble gas radii for the corresponding coordination environment and at the relevant conditions have been calculated to compare the modelled solubilities with those from experiments (symbols in each panel (Jackson et al., 2015; Krantz et al., 2019)).Note, that for the six membered ring site and the octahedral site two different Young's moduli have been calculated using a stiff structural model similar to the bulk structure and a flexible structural unit model that fits the experimental values.

coordination (green and orange symbols, Fig. 5a and b) are close to those of these vacancies (maxima of the green dashed and orange lines, Fig. 5a and b). In order to fit the model to the experimental data the maximal solubilities c_0 for these sites have been adjusted to $5 * 10^{-8}$ and $5 * 10^{-9}$ mol/g, respectively and the effective site stiffness parameters E_m was lowered to 10 GPa. This value is significantly lower than the computed one ($E_m = 87$ GPa) using the bulk and shear moduli reported for the bulk structure. Such a low stiffness parameter would imply a high flexibility of the host site, which is compatible with a host site built from six-fold membered rings of SiO_4 tetrahedra that are connected via corners. Indeed, in the serpentine structures or related hydrous mineral structures such as amphiboles that contain six-membered rings of SiO_4 thetrahedra, the corner sharing tetrahedral units can easily rotate. The flexibility of this structural sub-unit is evidenced by its much lower bulk moduli (38 GPa for amphibole) compared to the bulk modulus of the crystal structure (95 GPa for amphibole) (Comboni et al., 2018).

In contrast, a very low stiffness for the octahedral site, which is required to accommodate large noble gas atoms, is less realistic. Indeed, in antigorite, all octahedra are arranged in a layer and interconnected *via* edges. This already highly compact atomic arrangement induces a high stiffness, which is expected to be similar to the overall stiffness of the bulk structure (in the case of serpentine 87 GPa). For example, the bulk modulus of octahedral units in amphibole has been shown to be similar to the bulk modulus of the crystal structure (Comboni et al., 2018). Based on these arguments, the void spaces between the six membered rings have been considered as favourable incorporation sites for heavy noble gases while the octahedral vacancies have been excluded.

Even though four-fold coordinated Ne, Ar, Kr and Xe exhibit radii (blue symbols Fig. 5c) that are comparable to those of tetrahedral vacancies (maximum of the blue dashed line Fig. 5c), such an incorporation mechanism would imply higher solubilities for Ar and Kr. Therefore, it would fail to reproduce the solubility patterns observed experimentally. A large difference between the radii of light noble gases (He, Ne) and the radius of the voids between the six-fold membered rings is revealed in the model (Fig. 5a). This is unfavourable to their incorporation in this site. In addition, the reported solubility trend for He and Ne with $c_{He} > c_{Ne}$ cannot be reproduced by considering this incorporation mechanism. Based on the small radii of light noble gases, the observed solubilities can only be explained if He and Ne enter in a vacancy site with a radius of about 1 Å. Such a site is found between hydrogen atoms and the overlying SiO_4 tetrahedra (Fig. 5d). In serpentine, hydrogen atoms are bounded to oxygen atoms belonging to MgO_6 polyhedra in the octahedral layers and connected *via* weak van der Waals bonds to an oxygen atom belonging to a SiO_4 tetrahedron in the overlying tetrahedral sheet. Despite the fact that the ionization energies for He and Ne are the highest among the noble gases, their atomic shells can be polarized. At low pressure pure He and pure Ne are in the liquid state and their atoms are connected via weak van der Waal bonds. Moreover, stable van der Waals compounds such as NaHe or $He(N_2)_{11}$ have been reported in the pressure range between 7 and 15 GPa (Vos et al., 1992; Dong et al., 2017). For He-Na compounds reported by Dong et al. (2017) He enters as polarization buffer in the structure. This suggests that the hydrogen site in serpentine is a good candidate to trap He and Ne as polarization buffers. To fit the experimental data, the calculated site stiffness E_m of 87 GPa and a maximal solubilities c_0 of $3 * 10^{-9}$ mol/g was used. The incorporation of He and Ne in the hydrogen site can also reproduce the experimentally observed solubility relation: $c_{He} > c_{Ne}$. This could be explained by the similarities between the radius of a He atom and, the radius of the hydrogen site. In contrast, the radius of a Ne atom exhibits a greater mismatch to the hydrogen site radius. It is worth noting that the large uncertainties in reported Ne concentrations by Jackson et al. (2015) do not allow a clear assessment of its incorporation site. Despite its higher solubility in serpentine at hydrothermal conditions, He exhibits a higher diffusivity than Ne (Wang et al., 2020). This, in turn, leads to its preferential loss from serpentine during subduction which may explain the observations from natural samples (Kendrick et al., 2011).

4.4. Noble gas solubilities in antigorite at mantle wedge conditions (2 GPa and 773 K)

The LSM modelling was also employed to predict the solubilities (Henry's constants) of Ar, Kr and Xe in antigorite at the *P-T* conditions of the mantle wedge (2 GPa and 773 K). To this end, the noble gas radii were calculated using the thermal equation of state parameters listed in Table 4. It is worth noting that Ne was not included in this calculation because the EOS parameters from the literature are not sufficiently accurate in the relevant low *P-T* regime. For instance, Ne radii obtained using the EOS data reported in Dewaele et al. (2008) resulted in unrealistically large values. The effective site stiffness E_m for the void space between the six-membered ring site was set to its calculated value using the thermal EOS of the bulk structure (i.e. 115 GPa) and its maximal solubility was kept constant ($c_0 = 5 * 10^{-8}$ mol/g). The noble gas solubilities were derived using the calculated noble gases radii and the adjustment of the solubility curve, i.e., for Ar $c = 10^{-27}$ mol/g/bar; Kr $c = 8 * 10^{-26}$ mol/g/bar and Xe $c = 3 * 10^{-24}$ mol/g/bar; see Fig. 6. These values indicate a significant reduction of solubility values for Ar, Kr and Xe at mantle wedge conditions compared to those at hydrothermal conditions ($2.95 * 10^{-10}$ mol/g/bar for ^{36}Ar, $1.25 * 10^{-9}$ mol/g/bar for ^{84}Kr, and $3.6 * 10^{-9}$ mol/gbar for ^{130}Xe according to Krantz et al., 2019). This finding is in agreement with the observed reduced concentrations of heavy noble gases in natural antigorite-serpentinites (Kendrick et al., 2011) compared to lizardite/chrystolie bearing seafloor serpentines (Kendrick et al., 2013).

Through this model, a qualitative comparison of solubility trends in antigorite with increasing degree of subduction zone metamorphose could be obtained. This suggests lower solubilities in antigorite at mantle wedge conditions than at hydrothermal conditions and an increase in Kr and Xe solubilities relative to Ar. These findings are in excellent agreement with observations from natural samples Kendrick et al. (2011, 2013). These experimental data reveal a significant increase in the bond strength of heavy noble gases with pressure (section 2.2), which may explain their preferential retention in solid phases during mineral-fluid reactions in the mantle wedge. These results are also in agreement with the calculated diffusivities of noble gases in antigorite which decrease with the atomic radius (Wang et al., 2020). Wang et al. (2020) further demonstrated that at subduction zone conditions (at constant pressure of 3 GPa and upon heating), due to diffusion, structurally incorporated Xe and Kr in antigorite would be lost at higher temperatures than Ar. However, Wang et al. (2020) predicted an unfractionated loss of the originally contained noble gases Ar/Kr/Xe during antigorite breakdown because the temperature for diffusive loss of Ar/Kr/Xe exceeds the stability temperature of antigorite. Our LSM clearly demonstrates a lower compatibility of Ar than Xe in the six-membered ring sites in antigorite. Indeed, because of the smaller radii of Ar (1.96 Å) compared to Xe (2.01 Å), it displays a greater radii mismatch to the ideal host radii of the six-membered ring (2.5 Å) (see Fig. 6). The lower compatibility of Ar relatively to Xe may explain the high Ar versus Xe concentrations reported for the first breakdown fluids forming during antigorite dehydration (Kendrick et al., 2011). The noble gas concentrations calculated from the solubility data shown in Fig. 6, and assuming partial pressures of noble gases similar to those in seawater, are $1.1 * 10^{-32}$ mol/g; $3 * 10^{-32}$ mol/g and $9.7 * 10^{-33}$ mol/g for Ar^{36}, Kr^{84}, Xe^{130}, respectively. While the predicted absolute concentrations are not in agreement with those reported in a study focused on noble gas abundances in natural antigorite-serpentinites (Kendrick et al., 2011), the general noble gas concentrations trend with $c_{Ar} \geq c_{Kr} > c_{Xe}$ is preserved, i.e., according to Kendrick et al. (2011) Ar^{36}, Kr^{84} and Xe^{130} concentrations vary between 10^{-13}–10^{-11} mol/g, 10^{-13}–10^{-15}mol/g and 10^{-14}–10^{-16} mol/g, respectively. The discrepancies in terms of absolute concentrations could arise because the

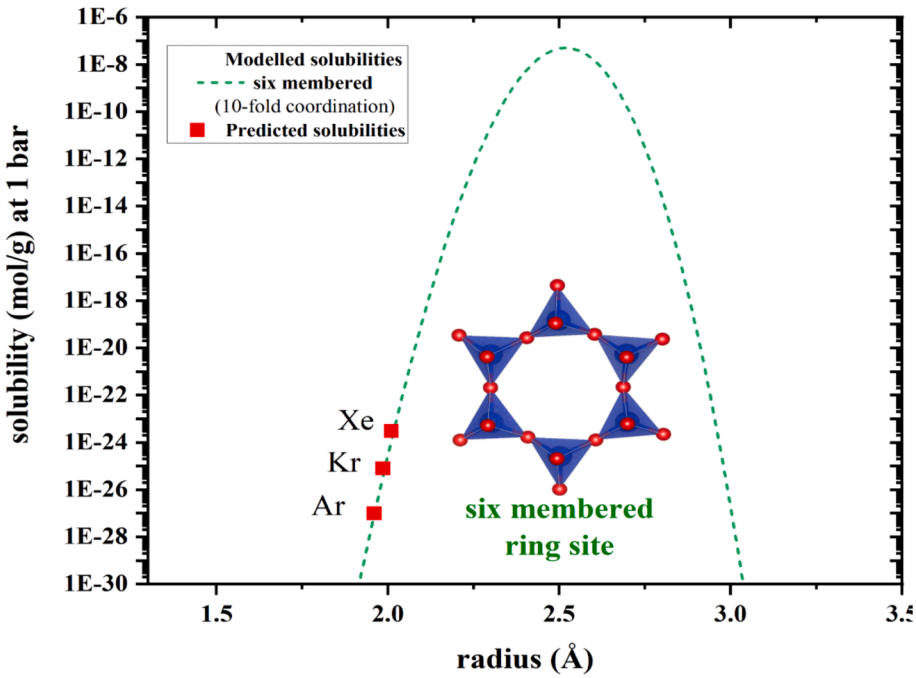

Fig. 6. Solubility trends (Henry's constants at 1 bar) at 2 GPa and 773 K as a function of the noble gas radius obtained from the LSM and the void space between the six-membered SiO_4 rings (green dashed line) in antigorite. Uncertainties on noble gas radii dimensions are within the symbol size.

calculated values of Henry's constants for noble gases in the present LSM model strongly depend on the input values *Em* and c_0. Especially the value of *Em* may be lower than the one assumed. A lower *Em* value would lead to higher predicted Henry's constants and thus absolute concentrations. Indeed, open six-membered ring sites in hydrous minerals may exhibit lower compressibilities and lower shear moduli than those of the bulk structure and may preserve a high flexibility at high pressure. For example, the bulk modulus of the six-fold membered ring in Amphibole has been determined to be 38 GPa, while the bulk structure represents a bulk modulus of 95 GPa (Comboni et al., 2018). Considering these values and assuming a similar relation between the shear modulus of the bulk structure and the six-membered ring site, we obtained a *Em* value of 20 GPa for antigorite at 2 GPa. This leads to Henry's constants of 10^{-12}, 10^{-11} and 30^{-10} for Ar^{36}, Kr^{84} and Xe^{130}, and corresponding concentrations of 1.1 * 10^{-17}, 2.5 * 10^{-22} and 4.9 * 10^{-23}. Another reason for the discrepancies in terms of absolute and relative concentrations between Ar, Kr and Xe may arise from out-of-equilibrium natural enrichment processes. These scenarios are further elaborated below.

4.5. Noble gas retention during hydrothermal alteration of peridotite

The comparison of experimentally derived solubilities and those observed in natural samples can provide important insights into the nature of natural hydration processes. As pointed out previously by Kendrick et al. (2013), naturally observed elemental concentrations for noble gases exceed those predicted from experiments. Experimental works found partitioning coefficients K_i that range between 4 * 10^{-5} and 6 * 10^{-3} with K_i = [*mol/g* serpentine]/ [*mol/g* water] (Zaikowski and Schaeffer, 1979; Krantz et al., 2019). These values imply concentrations of 1.6 * 10^{-15} mol/g for ^{36}Ar, 2.4 * 10^{-16} mol/g for ^{84}Kr, and 5.3.10^{-18} mol/g for ^{130}Xe dissolved at equilibrium in serpentine during seawater serpentinization using the partial pressures of noble gases in seawater at 1 kbar (Krantz et al., 2019). In contrast, studies on seafloor serpentines reported much higher concentrations, i.e., 3 * 10^{-12} mol/g for ^{36}Ar, 9.6 * 10^{-14} for ^{84}Kr and 1.4 * 10^{-15} mol/g of ^{130}Xe (2011; Kendrick et al., 2013). The high concentrations observed in natural samples could eventually arise from the trapped fluid inclusions. However, all studied samples have been found to be inclusion free (Kendrick et al., 2013). Another argument against fluid inclusions are the higher Kr/Ar and Xe/Ar ratios of natural samples than those of seawater that exhibit a large variability.

The discrepancies between experimentally determined solubilities for serpentines at hydrothermal conditions and those measured in seafloor serpentines may be due to hybrid hydration processes that include both open and closed system hydration reactions illustrated in Fig. 7. In close systems with low water–rock (W/R) ratios, the incompatible element composition of a fluid would be entirely retained in the newly formed hydrous phases if they did not reach saturation levels (Fig. 7 top panel). In pure open systems, that correspond to an infinite W/R ratio, the noble gas composition in minerals would be at equilibrium solubilities and, therefore, is expected to be low and constant (Fig. 7 bottom panel, contact zone to the fluid (a)). The high variability of the noble gas concentrations and, therefore, noble gas/water ratios are neither compatible with pure open nor pure closed system hydration processes (Kendrick et al., 2013; Kobayashi et al., 2017).

Kendrick et al. (2013) have proposed that the variability of the observed elemental ratios could be a result of various degrees of equilibrations between the fluid and the newly formed hydrous phases. This would proceed *via* noble gases fractionation by adsorption/desorption and diffusion processes. This scenario is in good agreement with the results of the present study. Indeed, they show a direct relationship between experimentally observed solubility trends and the mechanism of noble gas incorporation under seafloor serpentinization conditions. This strongly supports that the experimentally determined Henry constants reflect true incorporation processes and that adsorption and desorption processes at these conditions may not be dominant. This also suggests that the observed variations in noble gas abundance ratios may arise from complex serpentinization reactions in ultramafic rocks that commonly involve the growth of multi- generations of serpentine at differing degrees of water activities (Fig. 7). Progressive serpentinization reactions in ultramafic rocks at abyssal conditions have been previously documented (Schwarzenbach et al., 2016). These rocks are characterized by several generations of serpentine bearing veins that replace mostly olivine and to a lesser extent pyroxene. With increasing degree of hydration, the vein width and mineralogy change from a

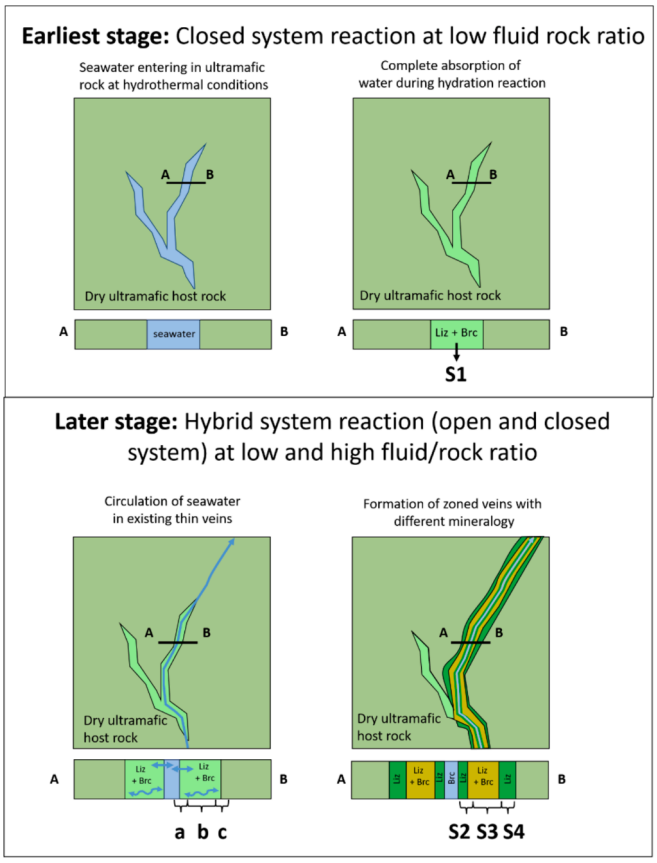

Fig. 7. Illustration of the hydrothermal alteration of a dry ultramafic rock at different alteration stages. Top panel: The earliest stage. Bottom panel: A later stage. The two stages illustrated here correspond to stages 1 and 3 described in Schwarzenbach et al. (2016) Fig. 6. The abbreviations Liz and Brc denote lizardite and brucite, respectively. For clarity cross-sections through the veins are shown below each figure to illustrate the mineralogy and noble gas composition. The mineralogical zoning of the vein shown in the bottom panel were extracted from Schwarzenbach et al. (2016). The retained noble gas concentrations and elemental patterns in lizardite at different alteration stages and in different zones of the veins are denoted as signature S1, S2, S3 and S4, respectively on the right panels. See main text for a detailed discussion.

homogenous serpentine-brucite bearing assemblage (small veins $>$ 20 μm) to a zoned mineralogy in which an assemblage of brucite and magnetite appear in the vein centres (large veins $>$ 50 μm). Schwarzenbach et al. (2016) have shown that in small veins an equilibrium assemblage consisting of olivine, serpentine and brucite is formed. This implies a complete consumption of water in the early fractures (Fig. 7 top panel). In more evolved zoned veins, the water activity changes significantly from the vein rim to its centre (highest water activity in the centre that decreases towards the contact zone with olivine) (Fig. 7 bottom panel).

These observations imply that during the first stages of serpentinization closed system reactions may occur and the noble gas signature (elemental patterns and isotopic composition) of the fluid may be entirely absorbed by newly formed serpentine (Signature S1 in the top panel of Fig. 7). This results in higher noble gas concentrations in natural serpentine samples than predicted from solubility experiments. Upon further serpentinization noble gas bearing fluids percolate from the vein centre between serpentine and brucite grains towards the olivine contact rim. The presence of these fluids could lead to a re-equilibration of the noble gases stored in serpentine formed during the first stage. Since water activities are low in these zones, any release of noble gases from these serpentines would increase quickly their partial pressures in the small amounts of fluids. This mechanism would therefore preserve part of the high noble gas concentrations in first-stage serpentines (Fig. 7 bottom panel, zone (b) and signature S3). Finally, these fluids that are charged potentially with a higher concentration of noble gases would be entirely consumed to replace olivine with second-stage serpentine. Again, this implies the complete consumption of the incompatible elements signature. The higher compatibility of Kr and Xe in serpentine relatively to Ar and the higher diffusivity of Ar than that of Kr and Xe, may progressively induce higher than seawater Kr/Ar and Xe/Ar ratios in the first-stage serpentines. These processes would lead to an enrichment of the light noble gases in fluids percolating towards the olivine rim and, therefore, of later stage serpentines forming from these fluids (Fig. 7 bottom panel zone (c) and signature S4). These reactions contrast with those in the vein centres that occur concomitantly at high water activities and that may resemble open system reactions. The high fluid flux and, therefore, high-water activity in the vein centre may induce equilibrium noble gas concentrations in serpentine close to this region (Fig. 7 bottom panel zone (a) and signature S2).

Apart from the main serpentine minerals, serpentine product phases such as brucite and magnetite may be also important for the transport of noble gases and their high concentrations in serpentinized rocks. The present knowledge of noble gas solubilities in these phases remains incomplete. Only one study has reported high noble gas solubilities in magnetite that are up to one order of magnitude higher than those of serpentine (Lancet and Anders, 1973), while noble gas solubilities in brucite have not been yet investigated. Magnetite may contribute to the high noble gas concentrations of serpentinites despite being a minor phase. Another important factor for the noble gas concentrations of serpentinites may be chemical effects on noble gas solubilities in serpentine. For example, Kendrick et al. (2013) have shown that Cl and Ar concentrations may be coupled and increase with increasing degree of serpentinization. Finally, experimental data on noble gas solubilities at mantle wedge conditions and at high noble gas partial pressure would be required to provide better insights in the fluid release and rehydration processes at such conditions through comparison with natural samples.

5. Conclusions

This study aimed at providing insights into the retention mechanism of noble gases in hydrous subduction zone minerals and at understanding better the origins of present discrepancies in reported noble gas solubilities and concentrations from field and experimental studies. To this end, we performed crystal chemical modeling to evaluate the incorporation mechanism of noble gases and their solubilities in serpentine minerals along subduction zone geotherms. Therefore, we determined the thermo-elastic properties and melting curve of solid xenon at high P/T conditions (up to 60 GPa and 728 K) using combined X-ray diffraction and X-ray absorption spectroscopy. A large number of data points (585) have been collected to characterize the weak temperature response of xenon. In the investigated temperature range, it was established that the pressure term is dominant above 10 GPa. At low pressures, volumetric changes are on the order of 0.6 % per 100 K. From the new dataset, the zero-charged atomic radii evolution of xenon have been determined at subduction zone conditions. The incorporation mechanism and solubility behaviour of noble gases (He, Ne, Ar, Kr, Xe) was inferred from their thermo-elastic data and lattice strain modelling. These models suggest that light noble gases (He, Ne) are likely retained between the weak interlayer hydrogen–oxygen bonds, while heavy noble gases Ar, Kr and Xe enter favourably in the void space between six membered SiO_4 rings. At mantle wedge conditions, this model predicts lower solubilities and increasing Kr/Ar and Xe/Ar ratios, which conforms to observations from natural samples. Based on these new findings, it is suggested that the higher than experimentally predicted noble gas concentrations in natural rocks may be due to the complex multi-stage serpentinization reactions in ultra-mafic rocks that occur under a large range of water activities.

CRediT authorship contribution statement

A.D. Rosa: Writing – review & editing, Writing – original draft, Visualization, Validation, Supervision, Project administration, Methodology, Investigation, Formal analysis, Data curation, Conceptualization. **F. Zecchi:** Writing – review & editing, Software, Formal analysis. **P. Condamine:** Writing – review & editing, Methodology, Data curation. **M.A. Bouhifd:** Writing – review & editing, Resources, Data curation, Conceptualization. **J.E.F.S. Rodrigues:** Writing – review & editing, Data curation. **E. Mijit:** Writing – review & editing, Data curation. **T. Irifune:** Writing – review & editing, Resources. **O. Mathon:** Writing – review & editing, Resources. **G. Garbarino:** Writing – review & editing, Resources. **M. Mezouar:** Writing – review & editing, Formal analysis. **A. Dewaele:** Writing – review & editing, Methodology, Formal analysis, Data curation. **N. Ishimatsu:** Writing – review & editing, Formal analysis, Data curation.

Declaration of competing interest

The authors declare that they have no known competing financial interests or personal relationships that could have appeared to influence the work reported in this paper.

Data availability

Data are available through Mendeley Data at https://doi.org/10.17632/f8t5f5wph6.1.

Acknowledgements

We deeply thank the editors for the fast editorial handling of the manuscript and David V. Bekaert as well as two anonymous reviewers for their constructive comments that greatly improved our manuscript. We also would like to thank the ESRF for providing beamtime, J. Jacobs (High-pressure laboratory) and the beamline teams of BM23 and ID15B for their help during the experiments.

Appendix A. Supplementary material

Supplementary material to this article can be found online at https://doi.org/10.1016/j.gca.2024.06.001.

References

Anderson, O.L., Isaak, D.G., Yamamoto, S., 1989. Anharmonicity and the equation of state for gold. J. Appl. Phys. 65, 1534–1543.
Anderson, M.S., Swenson, C.A., 1975. Experimental equations of state for rare-gas solids. J. Phys. Chem. Solids 36, 145–162.
Asaumi, K., 1984. High-pressure X-ray-diffraction study of solid xenon and its equation of state in relation to metallization transition. Phys. Rev. B 29, 7026–7029.
Auzende, A.L., Guillot, S., Devouard, B., Baronnet, A., 2006. Serpentinites in an Alpine convergent setting: effects of metamorphic grade and deformation on microstructures. Eur. J. Mineral. 18, 21–33.
Ballentine, C.J., Holland, G., 2008. What CO_2 well gases tell us about the origin of noble gases in the mantle and their relationship to the atmosphere. Phil. Trans. R. Soc. A 366, 4183–4203.
Blundy, J., Wood, B., 2003. Partitioning of trace elements between crystals and melts. Earth Planet. Sci. Lett. 210, 383–397.
Bouhifd, M.A., Jephcoat, A.P., 2006. Aluminium control of argon solubility in silicate melts under pressure. Nat. 439, 961–964.
Bouhifd, M.A., Jephcoat, A.P., Porcelli, D., Kelley, S.P., Marty, B., 2020. Potential of Earth's core as a reservoir for noble gases: case for helium and neon. Geochem. Perspect. Lett. 15, 15–18.
Brooker, R.A., Du, Z., Blundy, J.D., Kelley, S.P., Allan, N.L., Wood, B.J., Chamorro, E.M., Wartho, J.A., Purton, J.A., 2003. The 'zero charge' partitioning behaviour of noble gases during mantle melting. Nat. 423, 738–741.
Capitani, G.C., Mellini, M., 2006. The crystal structure of a second antigorite polysome (m = 16), by single-crystal synchrotron diffraction. Am. Mineral. 91, 394–399.
Chamorro, E.M., Brooker, R.A., Wartho, J.A., Wood, B.J., Kelley, S.P., Blundy, J.D., 2002. Ar and K partitioning between clinopyroxene and silicate melt to 8 GPa. Geochim. Cosmochim. Acta 66, 507–519.
Chauvel, C., Hofmann, A.W., Vidal, P., 1992. Himu Em - the French-Polynesian Connection. Earth Planet. Sci. Lett. 110, 99–119.
Chavrit, D., Burgess, R., Sumino, H., Teagle, D.A.H., Droop, G., Shimizu, A., Ballentine, C.J., 2016. The contribution of hydrothermally altered ocean crust to the mantle halogen and noble gas cycles. Geochim. Cosmochim. Acta 183, 106–124.
Comboni, D., Lotti, P., Gatta, G.D., Merlini, M., Liermann, H.-P., Frost, D.J., 2018. Pargasite at high pressure and temperature. Phys. Chem. Miner. 45, 259–278.
Crepisson, C., Blanchard, M., Lazzeri, M., Balan, E., Sanloup, C., 2018a. New constraints on Xe incorporation mechanisms in olivine from first-principles calculations. Geochim. Cosmochim. Acta 222, 146–155.
Crepisson, C., Sanloup, C., Cormier, L., Blanchard, M., Hudspeth, J., Rosa, A.D., Mathon, O., Irifune, T., 2018b. Kr environment in feldspathic glass and melt: A high pressure, high temperature X-ray absorption study. Chem. Geol. 493, 525–531.
Cynn, H., Yoo, C.S., Baer, B., Iota-Herbei, V., McMahan, A.K., Nicol, M., Carlson, S., 2001. Martensitic fcc-to-hcp transformation observed in xenon at high pressure. Phys. Rev. Lett. 86, 4552–4555.
Deschamps, F., Godard, M., Guillot, S., Hattori, K., 2013. Geochemistry of subduction zone serpentinites: a review. Lithos 178, 96–127.
Dewaele, A., Datchi, F., Loubeyre, P., Mezouar, M., 2008. High pressure–high temperature equations of state of neon and diamond. Phys. Rev. B 77, 094106.
Dewaele, A., Loubeyre, P., Dumas, P., Mezouar, M., 2012. Oxygen impurities reduce the metallization pressure of xenon. Phys. Rev. B 86, 014103.
Dewaele, A., Rosa, A.D., Guignot, N., 2019. Argon-neon binary diagram and $ArNe_2$ Laves phase. J. Chem. Phys. 151, 124708.
Dewaele, A., Rosa, A.D., Guignot, N., Andrault, D., Rodrigues, J.E.F.S., Garbarino, G., 2021. Stability and equation of state of face-centered cubic and hexagonal close packed phases of argon under pressure. Sci. Rep. 11, 15192.
Dong, X., Oganov, A.R., Goncharov, A.F., Stavrou, E., Lobanov, S., Saleh, G., Qian, G.-R., Zhu, Q., Gatti, C., Deringer, V.L., Dronskowski, R., Zhou, X.-F., Prakapenka, V.B., Konôpková, Z., Popov, I.A., Boldyrev, A.I., Wang, H.-T., 2017. A stable compound of helium and sodium at high pressure. Nat. Chem. 9, 440–445.
Errandonea, D., Schwager, B., Boehler, R., Ross, M., 2002. Phase behavior of krypton and xenon to 50 GPa. Phys. Rev. B 65, 214110.
Fenichel, H., Serin, B., 1966. Low-temperature specific heats of solid neon and solid xenon. Phys. Rev. 142, 490–495.
Gannarelli, C.M.S., Alfè, D., Gillan, M.J., 2005. The axial ratio of hcp iron at the conditions of the Earth's inner core. Phys. Earth Planet. Inter. 152, 67–77.
Gonzalez-Platas, J., Alvaro, M., Nestola, F., Angel, R., 2016. EosFit7-GUI: a new graphical user interface for equation of state calculations, analyses and teaching. J. Appl. Crystallogr. 49, 1377–1382.
Hanyu, T., Kaneoka, I., Nagao, K., 1999. Noble gas study of HIMU and EM ocean island basalts in the Polynesian region. Geochim. Cosmochim. Acta 63, 1181–1201.
Heber, V.S., Brooker, R.A., Kelley, S.P., Wood, B.J., 2007a. Crystal-melt partitioning of noble gases (helium, neon, argon, krypton, and xenon) for olivine and clinopyroxene. Geochim. Cosmochim. Acta 71, 1041–1061.
Heber, V.S., Brooker, R.A., Kelley, S.P., Wood, B.J., 2007b. Crystal–melt partitioning of noble gases (helium, neon, argon, krypton, and xenon) for olivine and clinopyroxene. Geochim. Cosmochim. Acta 71, 1041–1061.
Holland, G., Ballentine, C.J., 2006. Seawater subduction controls the heavy noble gas composition of the mantle. Geochim. Cosmochim. Acta 70, A259–A.
Holland, G., Cassidy, M., Ballentine, C.J., 2009. Meteorite Kr in earth's mantle suggests a late accretionary source for the atmosphere. Science 326, 1522–1525.
Ishimatsu, N., Matsumoto, K., Maruyama, H., Kawamura, N., Mizumaki, M., Sumiya, H., Irifune, T., 2012. Glitch-free X-ray absorption spectrum under high pressure obtained using nano-polycrystalline diamond anvils. J. Synchrotron Radiat. 19, 768–772.
Jackson, C.R.M., Parman, S., Kelley, S.P., Cooper, R.F., 2013. Noble gas transport into the mantle facilitated by high solubility in amphibole. Nat. Geosci. 6, 562–565.
Jackson, C.R.M., Parman, S.W., Kelley, S.P., Cooper, R.F., 2015. Light noble gas dissolution into ring structure-bearing materials and lattice influences on noble gas recycling. Geochim. Cosmochim. Acta 159, 1–15.
Jackson, C.R.M., Williams, C.D., Du, Z.X., Bennett, N.R., Mukhopadhyay, S., Fei, Y.W., 2021. Incompatibility of argon during magma ocean crystallization. Earth Planet. Sci. Lett. 553, 116598.
Jephcoat, A.P., 1998. Rare-gas solids in the Earth's deep interior. Nat. 393, 355–358.
Kendrick, M.A., Scambelluri, M., Honda, M., Phillips, D., 2011. High abundances of noble gas and chlorine delivered to the mantle by serpentinite subduction. Nat. Geosci. 4, 807–812.
Kendrick, M.A., Honda, M., Pettke, T., Scambelluri, M., Phillips, D., Giuliani, A., 2013. Subduction zone fluxes of halogens and noble gases in seafloor and forearc serpentinites. Earth Planet. Sci. Lett. 365, 86–96.
Kendrick, M.A., Hemond, C., Kamenetsky, V.S., Danyushevsky, L., Devey, C.W., Rodemann, T., Jackson, M.G., Perfit, M.R., 2017. Seawater cycled throughout Earth's mantle in partially serpentinized lithosphere. Nat. Geosci. 10, 222–228.
Kendrick, M.A., Scambelluri, M., Hermann, J., Padron-Navarta, J.A., 2018. Halogens and noble gases in serpentinites and secondary peridotites: Implications for seawater subduction and the origin of mantle neon. Geochim. Cosmochim. Acta 235, 285–304.
Khriachtchev, L., Pettersson, M., Runeberg, N., Lundell, J., Räsänen, M., 2000. A Stable Argon Compound. Nat. 406, 874–876.
Klotz, S., Chervin, J.C., Munsch, P., Le Marchand, G., 2009. Hydrostatic limits of 11 pressure transmitting media. J. Phys. D: Appl. Phys. 42, 075413–075420.
Kobayashi, M., Sumino, H., Nagao, K., Ishimaru, S., Arai, S., Yoshikawa, M., Kawamoto, T., Kumagai, Y., Kobayashi, T., Burgess, R., Ballentine, C.J., 2017. Slab-derived halogens and noble gases illuminate closed system processes controlling

volatile element transport into the mantle wedge. Earth Planet. Sci. Lett. 457, 106–116.
Krantz, J.A., Parman, S.W., Kelley, S.P., 2019. Recycling of heavy noble gases by subduction of serpentinite. Earth Planet. Sci. Lett. 521, 120–127.
Krstulović, M., Rosa, A.D., Sanchez, D.F., Libon, L., Albers, C., Merkulova, M., Grolimund, D., Irifune, T., Wilke, M., 2022. Effect of temperature on the densification of silicate melts to lower Earth's mantle conditions. Phys. Earth Planet. Inter. 323, 106823.
Lafay, R., Deschamps, F., Schwartz, S., Guillot, S., Godard, M., Debret, B., Nicollet, C., 2013. High-pressure serpentinites, a trap-and-release system controlled by metamorphic conditions: example from the Piedmont zone of the western Alps. Chem. Geol. 343, 38–54.
Lancet, M.S., Anders, E., 1973. Solubilities of noble-gases in magnetite - implications for planetary gases in meteorites. Geochim. Cosmochim. Acta 37, 1371–1388.
Letoullec, R., Pinceaux, J.P., Loubeyre, P., 1988. The membrane diamond anvil cell: a new device for generating continuous pressure and temperature variations. High Pressure Res. 1, 77–90.
Lutterotti, L., Matthies, S., Wenk, H.R., Schultz, A.S., Richardson, J.W., 1997. Combined texture and structure analysis of deformed limestone from time-of-flight neutron diffraction spectra. J. Appl. Phys. 81, 594–600.
Ma, Y., Somayazulu, M., Shen, G., Mao, H.-K., Shu, J., Hemley, R.J., 2004. In situ X-ray diffraction studies of iron to Earth-core conditions. Phys. Earth Planet. Inter. 143–144, 455–467.
Mao, H.K., Wu, Y., Chen, L.C., Shu, J.F., Jephcoat, A.P., 1990. Static compression of iron to 300 GPa and $Fe_{0.8}Ni_{0.2}$ alloy to 260 GPa: Implications for composition of the core. J. Geophys. Res. Solid Earth 95, 21737–21742.
Mathon, O., Beteva, A., Borrel, J., Bugnazet, D., Gatla, S., Hino, R., Kantor, I., Mairs, T., Munoz, M., Pasternak, S., Perrin, F., Pascarelli, S., 2015. The time-resolved and extreme conditions XAS (TEXAS) facility at the European Synchrotron Radiation Facility: the general-purpose EXAFS bending-magnet beamline BM23. J. Synchrotron Radiat. 22, 1548–1554.
Matsuda, J., Nagao, K., 1986. Noble-gas abundances in a deep-sea sediment core from eastern equatorial pacific. Geochem. J. 20, 71–80.
Miao, M.S., Wang, X.L., Brgoch, J., Spera, F., Jackson, M.G., Kresse, G., Lin, H.Q., 2015. Anionic chemistry of noble gases: formation of Mg-NG (NG = Xe, Kr, Ar) compounds under pressure. J. Am. Chem. Soc. 137, 14122–14128.
Moreira, M., 2013. Noble gas constraints on the origin and evolution of earth's volatiles. Geochem. Perspect. 2, 229–403.
Moreira, M., Kunz, J., Allegre, C., 1998. Rare gas systematics in popping rock: isotopic and elemental compositions in the upper mantle. Science 279, 1178–1181.
Moreira, M., Raquin, A., 2007. The origin of rare gases on Earth: the noble gas 'subduction barrier' revisited. C. r. Geosci. 339, 937–945.
Mukhopadhyay, S., Parai, R., 2019. Noble gases: a record of earth's evolution and mantle dynamics. Annu. Rev. Earth Planet. Sci. 47, 389–419.
Ohtani, E., 2020. The role of water in Earth's mantle. Natl. Sci. Rev. 7, 224–232.
Parai, R., Mukhopadhyay, S., 2015. The evolution of MORB and plume mantle volatile budgets: Constraints from fission Xe isotopes in Southwest Indian Ridge basalts. Geochem., Geophys Geosysts. 16, 719–735.
Péron, S., Moreira, M., 2018. Onset of volatile recycling into the mantle determined by xenon anomalies. Geochem. Perspect. Lett. 9, 21–25.
Péron, S., Mukhopadhyay, S., 2022. Pre-subduction mantle noble gas elemental pattern reveals larger missing xenon in the deep interior compared to the atmosphere. Earth Planet. Sci. Lett. 593, 117655.
Peto, M.K., Mukhopadhyay, S., Kelley, K.A., 2013. Heterogeneities from the first 100 million years recorded in deep mantle noble gases from the Northern Lau Back-arc Basin. Earth Planet. Sci. Lett. 369, 13–23.
Poli, S., Schmidt, M.W., 2002. Petrology of subducted slabs. Annu. Rev. Earth Planet. Sci. 30, 207–235.
Poręba, T., Comboni, D., Mezouar, M., Garbarino, G., Hanfland, M., 2023. Tracking structural phase transitions via single crystal x-ray diffraction at extreme conditions: advantages of extremely brilliant source. J. Phys.: Condens. Matter 35, 054001.
Raimondi, P., Benabderrahmane, C., Berkvens, P., Biasci, J.C., Borowiec, P., Bouteille, J.-F., Brochard, T., Brookes, N.B., Carmignani, N., Carver, L.R., Chaize, J.-M., Chavanne, J., Checchia, S., Chushkin, Y., Cianciosi, F., Di Michiel, M., Dimper, R., D'Elia, A., Einfeld, D., Ewald, F., Farvacque, L., Goirand, L., Hardy, L., Jacob, J., Jolly, L., Krisch, M., Le Bec, G., Leconte, I., Liuzzo, S.M., Maccarrone, C., Marchial, T., Martin, D., Mezouar, M., Nevo, C., Perron, T., Plouviez, E., Reichert, H., Renaud, P., Revol, J.-L., Roche, B., Scheidt, K.-B., Serriere, V., Sette, F., Susini, J., Torino, L., Versteegen, R., White, S., Zontone, F., 2023. The extremely brilliant source storage ring of the european synchrotron radiation facility. Commun. Phys. 6, 82.
Rapp, R.P., Irifune, T., Shimizu, N., Nishiyama, N., Norman, M.D., Inoue, J., 2008. Subduction recycling of continental sediments and the origin of geochemically enriched reservoirs in the deep mantle. Earth Planet. Sci. Lett. 271, 14–23.
Raquin, A., Moreira, M., 2009. Atmospheric Ar-38/Ar-36 in the mantle: Implications for the nature of the terrestrial parent bodies. Earth Planet. Sci. Lett. 287, 551–558.
Raquin, A., Moreira, M., Guillon, F., 2008. He, Ne and Ar systematics in single vesicles: Mantle isotopic ratios and origin of the air component in basaltic glasses. Earth Planet. Sci. Lett. 274, 142–150.
Ravel, B., Newville, M., 2005. ATHENA, ARTEMIS, HEPHAESTUS: data analysis for X-ray absorption spectroscopy using IFEFFIT. J. Synchrotron Radiat. 12, 537–541.
Reynard, B., Hilairet, N., Balan, E., Lazzeri, M., 2007. Elasticity of serpentines and extensive serpentinization in subduction zones. Geophys. Res. Lett. 34, L13307.
Romanenko, A.V., Rashchenko, S.V., Kurnosov, A., Dubrovinsky, L., Goryainov, S.V., Likhacheva, A.Y., Litasov, K.D., 2018. Single-standard method for simultaneous pressure and temperature estimation using Sm^{2+}:SrB_4O_7 fluorescence. J. Appl. Phys. 124, 165902.
Rosa, A.D., Garbarino, G., Briggs, R., Svitlyk, V., Morard, G., Bouhifd, M.A., Jacobs, J., Irifune, T., Mathon, O., Pascarelli, S., 2018. Effect of the fcc-hcp martensitic transition on the equation of state of solid krypton up to 140 GPa. Phys. Rev. B 97, 094115.
Rosa, A.D., Mathon, O., Torchio, R., Jacobs, J., Pasternak, S., Irifune, T., Pascarelli, S., 2019. Nano-polycrystalline diamond anvils: key devices for XAS at extreme conditions: their use, scientific impact, present status and future needs. High Pressure Res. 40, 65–81.
Rosa, A.D., Bouhifd, M.A., Morard, G., Briggs, R., Garbarino, G., Irifune, T., Mathon, O., Pascarelli, S., 2020. Krypton storage capacity of the Earth's lower mantle. Earth Planet. Sci. Lett. 532, 116032.
Rosa, A.D., Dewaele, A., Garbarino, G., Svitlyk, V., Morard, G., De Angelis, F., Krstulović, M., Briggs, R., Irifune, T., Mathon, O., Bouhifd, M.A., 2022. Martensitic fcc-hcp transformation pathway in solid krypton and xenon and its effect on their equations of state. Phys. Rev. B 105, 144103.
Roubinet, C., Moreira, M.A., 2018. Atmospheric noble gases in Mid-Ocean Ridge Basalts: Identification of atmospheric contamination processes. Geochim. Cosmochim. Acta 222, 253–268.
Sarda, P., 2004. Surface noble gas recycling to the terrestrial mantle. Earth Planet. Sci. Lett., 228, 1–2, 2004, 49–63.
Sarda, P., Moreira, M., Staudacher, T., 1999. Argon-lead isotopic correlation in Mid-Atlantic Ridge basalts. Science 283, 666–668.
Scambelluri, M., Cannao, E., Gilio, M., 2019. The water and fluid-mobile element cycles during serpentinite subduction. A review. Eur. J. Mineral. 31, 405–428.
Schwarzenbach, E.M., Caddick, M.J., Beard, J.S., Bodnar, R.J., 2016. Serpentinization, element transfer, and the progressive development of zoning in veins: evidence from a partially serpentinized harzburgite. Contrib. Mineral. Petrol. 171, 1–22.
Shcheka, S.S., Keppler, H., 2012. The origin of the terrestrial noble-gas signature. Nat. 490, 531–534.
Shen, G., Wang, Y., Dewaele, A., Wu, C., Fratanduono, D.E., Eggert, J., Klotz, S., Dziubek, K.F., Loubeyre, P., Fat'yanov, O.V., Asimow, P.D., Mashimo, T., Wentzcovitch, R.M.M., 2020. Toward an international practical pressure scale: A proposal for an IPPS ruby gauge (IPPS-Ruby2020). High Pressure Res. 40, 299–314.
Staudacher, T., Allègre, C.J., 1988. Recycling of oceanic-crust and sediments - the noble-gas subduction barrier. Earth Planet. Sci. Lett. 89, 173–183.
Steinle-Neumann, G., Stixrude, L., Cohen, R.E., Gülseren, O., 2001. Elasticity of iron at the temperature of the Earth's inner core. Nat. 413, 57–60.
Sumino, H., Burgess, R., Mizukami, T., Wallis, S.R., Holland, G., Ballentine, C.J., 2010. Seawater-derived noble gases and halogens preserved in exhumed mantle wedge peridotite. Earth Planet. Sci. Lett. 294, 163–172.
Takemura, K., Dewaele, A., 2008. Isothermal equation of state for gold with a He-pressure medium. Phys. Rev. B 78, 104119.
Thompson, A.E., Wolverton, C., 2011. First-principles study of noble gas impurities and defects in UO_2. Phys. Rev. B 84, 143111.
Trieloff, M., Kunz, J., Clague, D.A., Harrison, D., Allègre, C.J., 2000. The nature of pristine noble gases in mantle plumes. Science 288, 1036–1038.
Vos, W.L., Finger, L.W., Hemley, R.J., Hu, J.Z., Mao, H.K., Schouten, J.A., 1992. A high-pressure van der Waals compound in solid nitrogen-helium mixtures. Nat. 358, 46–48.
Wang, K., Lu, X., Brodholt, J.P., 2020. Diffusion of noble gases in subduction zone hydrous minerals. Geochim. Cosmochim. Acta 291, 50–61.
Yang, C., Inoue, T., Yamada, A., Kikegawa, T., Ando, J.-I., 2014. Equation of state and phase transition of antigorite under high pressure and high temperature. Phys. Earth Planet. Int. 228, 56–62.
Zaikowski, A., Schaeffer, O.A., 1979. Solubility of noble-gases in serpentine - implications for meteoritic noble-gas abundances. Earth Planet. Sci. Lett. 45, 141–154.
Zhang, Y.X., Xu, Z.J., 1995. Atomic radii of noble-gas elements in condensed phases. Am. Mineral. 80, 670–675.